SUBMITTED TO APJ. AUGUST 22, 2005
Preprint typeset using LaTeX style emulateapj v. 6/22/04

THE SPIN PERIODS AND ROTATIONAL PROFILES OF NEUTRON STARS AT BIRTH

CHRISTIAN D. OTT
Max-Planck-Institut für Gravitationsphysik, Albert-Einstein-Institut, Golm/Potsdam, Germany; cott@aei.mpg.de

ADAM BURROWS
Department of Astronomy and Steward Observatory, The University of Arizona, Tucson, AZ 85721; burrows@zenith.as.arizona.edu

TODD A. THOMPSON*
Astronomy Department and Theoretical Astrophysics Center, 601 Campbell Hall,
The University of California, Berkeley, CA 94720; thomp@astro.berkeley.edu

ELI LIVNE
Racah Institute of Physics, The Hebrew University, Jerusalem, Israel; eli@frodo.fiz.huji.ac.il

ROLF WALDER
Department of Astronomy and Steward Observatory, The University of Arizona, Tucson, AZ 85721; rwalder@as.arizona.edu
Submitted to ApJ. August 22, 2005

ABSTRACT

We present results from an extensive set of one- and two-dimensional radiation-hydrodynamic simulations of the supernova core collapse, bounce, and postbounce phases, and focus on the protoneutron star (PNS) spin periods and rotational profiles as a function of initial iron core angular velocity, degree of differential rotation, and progenitor mass. For the models considered, we find a roughly linear mapping between initial iron core rotation rate and PNS spin. The results indicate that the magnitude of the precollapse iron core angular velocities is the single most important factor in determining the PNS spin. Differences in progenitor mass and degree of differential rotation lead only to small variations in the PNS rotational period and profile. Based on our calculated PNS spins, at $\sim$200-300 milliseconds after bounce, and assuming angular momentum conservation, we estimate final neutron star rotation periods. We find periods of one millisecond and shorter for initial central iron core periods of below $\sim$10 s. This is appreciably shorter than what previous studies have predicted and is in disagreement with current observational data from pulsar astronomy. After considering possible spindown mechanisms that could lead to longer periods we conclude that there is no mechanism that can robustly spin down a neutron star from $\sim$1 ms periods to the "injection" periods of tens to hundreds of milliseconds observed for young pulsars. Our results indicate that, given current knowledge of the limitations of neutron star spindown mechanisms, precollapse iron cores must rotate with periods around 50-100 seconds to form neutron stars with periods generically near those inferred for the radio pulsar population.

Subject headings: Hydrodynamics, Neutrinos, Radiative Transfer, Stars: Evolution, Stars: Neutron, Stars: Supernovae: General, Pulsars: General, Stars: Rotation

1. INTRODUCTION

Neutron stars are formed in the core collapse of dying massive stars or (rarely) in the accretion-induced collapse (AIC) of O-Ne-Mg white dwarfs in binary systems. In both types of collapse events an electron-degenerate core is pushed over its effective Chandrasekhar mass. The collapse is halted only when the core density reaches $\sim 2 \times 10^{14}$ g cm^{-3} and nuclei undergo a phase transition to free nucleons. The equation of state (EOS) abruptly stiffens at that point and the core bounces, launching a hydrodynamic shock wave into the supersonically infalling outer core and leaving behind a hot and extended protoneutron star (PNS). The bounce shock stalls almost immediately and turns into an accretion shock due to a combination of neutrino losses, the ram pressure of the infalling mantle, and the dissociation of heavy nuclei into neutrons, protons and α particles. The subsequent evolution of the system to a potentially successful supernova explosion has been under detailed investigation for many decades now. The favored "delayed neutrino mechanism" (Bethe & Wilson 1985) relies on shock revival due to sufficient energy deposition by neutrinos in the so-called "gain region" behind the stalled shock. However, using numerical simulations that incorporate Boltzmann neutrino transfer and the best available physics, a number of efforts have shown that this mechanism does not succeed in spherical

*Hubble Fellow

symmetry (Mezzacappa et al. 2001; Liebendörfer et al. 2001; Rampp & Janka 2002; Thompson et al. 2003). In spherical symmetry, the bounce shock is not revived, though an increase of only ∼25% in the net energy deposition (all else being equal) would be sufficient to drive a successful explosion (Thompson et al. 2005). However, recent two-dimensional simulations (Herant et al. 1994; Burrows et al. 1995; Fryer & Heger 2000; Janka et al. 2003; Buras et al. 2003; Walder et al. 2005), and the first approximate three-dimensional simulations (Fryer & Warren 2004; Janka et al. 2005) indicate that indeed multi-dimensional phenomena such as postbounce convection and/or rotation might lead to the conditions needed for a successful explosion. In the same context, Thompson et al. (2005) performed simulations in spherical symmetry, including a 1D prescription for rotation, angular momentum transport, and viscous heating. A number of their more rapidly rotating models exploded due to the additional energy deposited behind the stalled shock by viscous dissipation.

It is, however, possible that only stars of masses less than ∼25-30 $M_\odot$ explode as supernovae, leaving neutron stars (Fryer 1999; Heger et al. 2003a). The fate of more massive progenitor stars is more uncertain and may be associated with under-energetic supernovae (Nomoto et al. 2005), hypernovae, gamma-ray bursts (GRBs), and/or black hole formation (Fryer 1999; Fryer & Kalogera 2001; Heger et al. 2003a). If shock revival and a strong supernova explosion result, no critical amount of mass is accreted onto the PNS. The PNS cools and contracts quasi-hydrostatically to its final radius of ∼10 - 15 km on a timescale of *tens* of seconds, radiating away $\sim 3 \times 10^{53}$ ergs in neutrinos (Burrows & Lattimer 1986; Keil & Janka 1995; Pons et al. 1999).

Long after the supernova explosion, the still young neutron star becomes visible to observers, possibly as a canonical rotation-powered radio pulsar (Kaspi & Helfand 2002). Observationally, it is often difficult to directly associate pulsars with supernova remnants (SNRs). This is partly due to the difference between the lifetimes of a typical pulsar (10^{6-7} years) and a SNR (10^{4-5} years) (Lyne & Graham-Smith 1998). In addition, pulsars have observed average space velocities of 200 - 500 km s^{-1} (Lyne & Lorimer 1994), most probably imparted to them during the supernova. These "pulsar kicks" may be a strong indication of the multi-dimensional nature of the supernova mechanism (Burrows & Hayes 1996; Lai et al. 2001; Fryer 2004; Scheck et al. 2004).

Observations of radio pulsars imply that the initial rotation rate of neutron stars is in the vicinity of tens to hundreds of milliseconds (Kaspi & Helfand 2002). The fastest known young pulsar is PSR J0537-6910 which is associated with SNR N157B and has a spin period of 16 ms and an age of ∼5 kyr. If one assumes a pulsar breaking index, n, less than or equal to 2 [1], a pulsar initial period $\lesssim$ 10 ms is obtained (Marshall et al. 1998). For the Crab pulsar (PSR B0531+21, P = 33 ms), n has been measured and because the year of the Crab's birth is known independently (1054 A.D.), a solid initial spin determination of $P_{initial}$ = 19 ms has been made (Kaspi & Helfand 2002).

The empirically determined initial spin periods of pulsars have to be matched to the theoretical models of stellar evolution, core collapse, supernova explosion, and neutron star cooling. Massive stars are suspected to rotate rigidly and rapidly during hydrogen burning on the main sequence. Their equatorial velocities are typically ∼200 km s^{-1}, which corresponds to ∼10% of their Keplerian break up speed (Fukuda 1982). Since there is no detailed empirical knowledge of the evolution of the angular momentum distribution inside an evolving star and because consistent multi-dimensional stellar evolutionary calculations have yet to be performed, stellar evolution theorists must rely on parameter-dependent, semi-phenomenological prescriptions to follow the angular momentum evolution of massive stars in their spherically symmetric models. Heger et al. (2000) have presented the first rotating presupernova stellar models that included a 1D prescription for angular momentum transport and centrifugal effects (the latter only up to the end of core carbon burning). These authors estimated the neutron star spin rate by assuming that the total angular momentum contained in the pre-collapse iron core is conserved during collapse and supernova phases and is deposited completely in a rigidly rotating neutron star of radius and moment of inertia (I) of ≈ 12 km and 0.35 M_{NS} R_{NS}^2, respectively (Lattimer & Prakash 2001). In this simple way, they estimated an initial neutron star period of ∼1 ms for their fiducial 20 $M_\odot$ (ZAMS) stellar model. Given the above observational data, this initial period is at least a factor of ten too short for the generic pulsar. Processes that could lead to an early spin-down of a young (proto)neutron star include: angular momentum redistribution by global hydrodynamic rotational instabilities (Centrella et al. 2001; Ott et al. 2005), r-modes and gravitational radiation back-reaction (Ho & Lai 2000; Lindblom et al. 2001; Watts & Andersson 2002; Arras et al. 2003), rotation-powered explosions (Akiyama et al. 2003; Akiyama & Wheeler 2005), viscous angular momentum transport due to convection, neutrino viscosity or dissipation of shear energy stored in differential rotation (Thompson et al. 2005), magneto-centrifugal winds (Thompson 2003a; Thompson et al. 2004), early magnetic-dipole radiation (Ostriker & Gunn 1969), late-time fall-back (Heger et al. 2005), and anisotropic neutrino emission (Janka 2004).

It is also possible that slowly spinning cores are the natural end-product of stellar evolution. Spruit & Phinney (1998) included angular momentum transport via magnetic processes that yielded such large neutron star periods (P ∼100 s) that the authors had to rely on subsequent spin-up by off-center birth kicks to obtain spin periods matching the observations. With a similar approach for magnetic angular momentum transport during stellar evolution and the simple neutron star spin estimate described above, Heger et al. (2003b) and Heger et al. (2005) obtained neutron star periods of ∼10 ms. However, given the differences in estimated iron core spin rates and angular momentum profiles in the literature and keeping in mind that the study of stellar evolution with rotation is still in its infancy, one should be cautious in accepting any of the recent estimates as a final answer. Too many open issues remain and can only be resolved by truly multi-dimensional stellar evolution studies in the future. Until then, rotating 1D evolutionary models are the only means we have of estimating the angular momentum distribution and spin rate of iron cores at the onset of core collapse. During the subsequent collapse evolution, the core spins up due to angular momentum conservation and — depending upon its initial distribution and amount of angu-

[1] A breaking index of 3 holds for pure magnetic dipole radiation and n < 2-3 is common for young pulsars (Lyne & Graham-Smith 1998).

lar momentum — becomes oblate due to rotational flattening. If the rotating core deviates significantly from spherical symmetry, a multi-dimensional treatment becomes indispensable to obtain reliable estimates of neutron star birth periods.

To date, only a small number of multi-dimensional supernova studies have addressed the neutron star spin question. Fryer & Heger (2000) performed smooth-particle hydrodynamics simulations with a gray, flux-limited diffusion scheme for radiative transfer of the neutrinos. They used the rotating progenitor model E15B of Heger et al. (2000) and estimated an initial spin period of the PNS (at the end of their simulation and assuming rigid rotation) on the order of 100 ms. It is, however, not clear how they defined the extent of the PNS. Taking the angular momentum contained in their PNS and following Heger et al. (2000) they obtained a neutron star spin period of $\sim$2 ms, even for a progenitor model that included an α-disk-like prescription for turbulent-viscous angular momentum redistribution. In their recent gray 3D smooth-particle radiation-hydrodynamics calculation, Fryer & Warren (2004) estimated neutron star spin periods by assuming that the angular momentum of the inner 1 $M_\odot$ is conserved as the PNS cools and contracts to a neutron star. For model E15A (Heger et al. 2000) they estimated in that way a neutron star period of 0.91 ms and for the slow "magnetic" 15 $M_\odot$ model of Heger et al. (2003b) a period of 17 ms. Ott et al. (2004) have performed purely hydrodynamic simulations with a detailed nuclear equation of state and realistic progenitor models and focused on the impact of rotation on the gravitational wave signatures of stellar core collapse. They argue that if gravitational waves of a core-collapse event were observed with sufficient precision it would be possible to infer details about the rotational configuration from the observations.

Using the code VULCAN/2D, Walder et al. (2005) performed a series of 2D multi-group, multi-species flux-limited diffusion radiation-hydrodynamics supernova simulations with the 11 $M_\odot$ (ZAMS) progenitor model of Woosley & Weaver (1995), which they artificially forced to rotate according to a rotation law that enforces constant angular velocity on cylindrical shells. Their focus was on the anisotropies in the neutrino-radiation field and in neutrino heating due to the rotational flattening of the postbounce core and they did not systematically analyze the final rotational configuration of their PNSs. In their 1D supernova simulations, Thompson et al. (2005) included the effects of rotation approximately and they studied the action of viscous processes in dissipating the strong rotational shear profile produced by core collapse in a range of progenitors and for different initial iron core periods. They showed that for rapidly rotating cores with postbounce periods of $\lesssim$ 4 ms, viscosity (presumably by magnetic torques, e.g. the magneto-rotational instability [MRI] or magneto-convection) can spin down the rapidly rotating PNSs by a factor of $\sim 2-3$ in the early postbounce epoch.

This paper is the first in a series of papers in which we plan to make progressively better estimates of neutron star birth periods and rotational configurations, connecting supernova theory with pulsar science. Here, we present the first systematic investigation of the mapping between initial iron core spin and the rotational configuration of neutron stars at birth carried out with state-of-the-art one- and two-dimensional radiation-hydrodynamics codes.

In §2, we describe the supernova codes SESAME and VULCAN/2D which we employ in this study. Section 3 reviews the progenitor model suite on which we are relying and discusses the rotation laws and mappings used. Section 4 describes our calculations in one and two spatial dimensions. In §5, we compare one-dimensional and two-dimensional simulations and assess the quality of the rotating one-dimensional models. In §6, based on the PNS structures that we find in our simulations, we estimate the final cold neutron star spin and discuss spindown mechanisms. Finally, in §7 we summarize our results and discuss them critically.

2. COMPUTATIONAL METHODS

2.1. *1-D, Spherically Symmetric Simulations*

Our spherically symmetric models are computed with the radiation-hydrodynamics algorithm SESAME[2], described in detail in Burrows et al. (2000) and Thompson et al. (2003). The hydrodynamics scheme is Lagrangean, Newtonian, and explicit. It is coupled to the EOS of Lattimer & Swesty (1991) (the LSEOS), using the implementation described in Thompson et al. (2003). The comoving Boltzmann equation for neutrinos is solved implicitly and to order v/c (where v is the matter velocity).

Thompson et al. (2005) have extended SESAME to approximately include the effects of rotation, as well as angular momentum transport by viscosity and local viscous heating. The strong negative shear profile ($d\Omega/d\ln r$) generated by core collapse implies that much of the region interior to the supernova shock is unstable by the generalized Solberg-Høiland criterion and, thus, to the magneto-rotational instability (MRI; Balbus & Hawley 1991, 1994; see also Akiyama et al. 2003). Under the assumption that magnetic torques provide the dominant viscosity in the PNS, by equating the shear and Maxwell stresses one derives that the shear viscosity should scale as $\xi \sim h^2\Omega$, where h is the pressure scale height. Following Thompson et al. (2005), we introduce an α-parameter (in analogy with studies of accretion) and take $\xi = \alpha h^2\Omega$. With this form for the viscosity the viscous heating rate scales as Ω^3. The viscous timescale is $\tau_{\rm visc} \sim (\alpha\Omega)^{-1}(r/h)^2$. If the MRI does operate in PNSs at birth, any seed magnetic field grows exponentially on a timescale $\sim \Omega^{-1}$. Although the saturation magnetic field strength is somewhat uncertain, to first approximation the toroidal magnetic field grows until $B_{{\rm sat},\,\phi} \sim (4\pi\rho)^{1/2} r\Omega$, which is of order $\sim 10^{16}$ G for $\rho = 10^{12}$ g cm^{-3}, $r \sim 40$ km, and a protoneutron star spin period of ~ 10 ms just after collapse (Akiyama et al. 2003). The poloidal magnetic energy density saturates at a value approximately an order of magnitude smaller than $B^2_{{\rm sat},\,\phi}/8\pi$ (e.g., Balbus & Hawley 1998).

All rotating 1D models (:1D suffix in the model name) are evolved with 500 mass zones, encompassing the progenitor iron core. Twenty energy groups are employed in the radiation transport per neutrino species. Models that include viscosity have an additional "v" added to their model name (see Table 1). All viscous models assume $\alpha = 0.1$. Viscosity is turned on at bounce and is assumed to act at all radii interior to the shock radius.

[2] **S**pherical **E**xplicit/Implicit **S**upernova **A**lgorithm for **M**ulti-Group/Multi-Angle **E**xplosion Simulations.

2.2. *2-D, Axisymmetric Simulations*

Our axisymmetric core-collapse supernova models are evolved using the 2D Newtonian, multi-species, multi-group, flux-limited (MGFLD) variant of the multi-species, multi-group, multi-angle, time-dependent radiation-hydrodynamics code VULCAN/2D (Livne et al. 2004). This variant has previously been used and described in the study of Walder et al. (2005). Its hydrodynamics module (Livne 1993) uses an Arbitrary Lagrangean-Eulerian scheme with remap and a scalar von Neumann-Richtmyer artificial viscosity scheme for shock handling. We employ the LSEOS, using the implementation described by Thompson et al. (2003).

Since VULCAN/2D uses an Eulerian grid, the specific angular momentum is advected with the flow in the same manner as linear momemtum components. In so doing, we maintain global angular momentum conservation by construction. Note that the axis in cylindrical coordinates is a singularity and, as such, is prone to slightly larger errors than can be expected elsewhere on the grid. In the past, we (Walder et al. 2005) have estimated such departures near the singularity for rotating models to be no more than $\sim$10% in any flow variable, and to be much smaller elsewhere.

Using the MGFLD variant of VULCAN/2D allows us to perform an extensive study that encompasses the evolution of many rotating models to times up to $\sim$300 ms after core bounce. However, one should bear in mind that MGFLD is only an approximation to full Boltzmann transport and differences with the more exact treatment will emerge in the neutrino semi-transparent and transparent regimes above the PNS surface. Inside the neutrinosphere of the PNS the two-dimensional MGFLD approach provides a very reasonable representation of the multi-species, multi-group neutrino radiation fields. The flux limiter used in this study is a vector version of that of Bruenn (1985), as discussed in Walder et al. (2005).

A key feature of VULCAN/2D is its ability to deal with arbitrarily shaped grids while using cylindrical coordinates in axisymmetry. The grid setup we use for this study is similar to the one depicted in Ott et al. (2004). All our models are evolved on the full 180 degrees of the symmetry domain. Those models from the simulations of Walder et al. (2005) are evolved with 80 evenly spaced angular zones and 130 logarithmically distributed radial zones out to 2000 km. All Walder et al. (2005) models are evolved with 8 neutrino energy groups for each neutrino species. Our previously unpublished models are evolved without exception with 16 energy groups per neutrino species, 120 angular and 220 radial zones out to 3000 km, and, for very massive presupernova cores, out to 5000 km. A resolution comparison study reveals local qualitative and quantitative differences between runs with different energy/spatial resolutions, but integral and global observables, such as the shock radius as a function of time turn out to be relatively independent of the resolution, at least at times up to $\sim$150 - 200 ms after bounce.

3. INITIAL MODELS

We use two sets of realistic supernova progenitor models from stellar evolutionary calculations as initial data for our simulations. The first set encompasses models s11, s15, and s20 (ZAMS mass of 11 $M_\odot$, 15 $M_\odot$, 20 $M_\odot$; solar metallicity) of Woosley & Weaver (1995). These models were evolved in spherical symmetry until the onset of iron core collapse. In Fig. 2, we compare the matter density profiles (panel (a)) and mass profiles (panel (b)) of the presupernova models. Note that models s11 and s15 have nearly identical structures out to $\sim$1000 km. The s20 model has a shallower density profile and a lower central density, but a more massive iron core ($\sim$1.9$M_\odot$, see Table 1).

On mapping to our simulation grids we introduce rotation using the rotation law,

$$\Omega(r) = \Omega_0 \left[1 + \left(\frac{r}{\mathrm{A}}\right)^2\right]^{-1}, \qquad (1)$$

where $\Omega_0 = 2\pi \mathrm{P}_0^{-1}$ is the angular velocity corresponding to the initial central rotation period P_0. A is a free parameter that determines the degree of differential rotation in our models. For $r \lesssim$ A, the initial rotation profile is roughly solid-body. According to the Poincaré-Wavre theorem, degenerate rotating fluid bodies have constant specific angular momentum on *cylinders* (see, e.g., Tassoul 1978). Hence, we choose *r* in eq. (1) to be the *cylindrical radial coordinate* ("cylindrical rotation") of the two-dimensional models that we evolve with VULCAN/2D. In spherical symmetry, the approximate treatment of rotation goes along with the assumption of constant angular momentum on *spherical* shells ("shellular rotation") and we interpret *r* as the *spherical radial coordinate* in all models evolved in spherical symmetry with SESAME. To compare "shellular" and "cylindrical" rotation laws, one of our two-dimensional models is set up to rotate initially with constant angular momentum on spherical shells. Figure 1 demonstrates that the above rotation law reasonably approximates the rotational profiles of the rotating presupernova models of Heger et al. (2000) if one chooses A$\sim$1000 km. Except for two models in which we investigate the effect of A $\sim \infty$, all other models of this set have A=1000 km. We name our models according to the following convention: [progenitor name]A[in km]P[P_0 in s][:evolution type]. For example, s11A1000P8.00:1Dv is a Woosley & Weaver (1995) 11 $M_\odot$ model with A = 1000 km and P_0 = 8.00 s that was evolved in one-dimension with viscous dissipation turned on after core bounce. Other evolution types are :1D (one-dimensional, no viscous dissipation), :2D (two-dimensional, "cylindrical rotation"), 2Ds (two-dimensional, "shellular rotation") and 2Dh (two-dimensional, "cylindrical rotation," purely hydrodynamic, no neutrino transfer). Table 1 details our choices of progenitor model, value of A, P_0, and evolution type for this model set. In particular, we choose the range of P_0 so that Keplerian rotational velocities are not attained anywhere during the numerical evolution, that is $\Omega(r,t) < \Omega_{\mathrm{Kepler}} = \sqrt{GM/r^3}$ for all *r* and *t*. In terms of the widely used rotation parameter β which is defined as the ratio of rotational kinetic to gravitational potential energy (T/|W|), this series models' precollapse values range from 7×10^{-5}% up to 0.88% for the fastest model.

The second set of progenitors ("Heger models" in the following) which we consider consists of models E15A, E20A (Heger et al. 2000) and m15b6 (Heger et al. 2005). These progenitor models were evolved to the onset of iron core collapse with the approximate treatment of rotation described by Heger et al. (2000), but centrifugal forces were included only until the end of core carbon burning. Model E15A and model E20A are relatively fast rotators with initial central periods of $\sim$1.5 and 2 seconds and values of β = T/|W| of $\sim$0.5% and

0.3%, respectively. In model m15b6, angular momentum redistribution by magnetic processes was included. This led to slow and more rigid rotation of its iron core, as can be inferred from Fig. 1. In Fig. 2, we compare the density and mass profiles of the "Heger models" with those of the nonrotating s11, s15, and s20 models. The slow m15b6 has very similar structure to the nonrotating s11 and s15 models. In the $15 M_\odot$ E15A model, rotational effects lead to a considerably more extended iron core with lower central density and shallower density stratification than in the nonrotating s15. Model E20A's structure, however, does not deviate significantly from that of the nonrotating s20.

The models are mapped onto our computational grids according to the same prescription presented for the first set: "shellular rotation" in 1D, "cylindrical rotation" for most two-dimensional models. In naming the models belonging to this set, we follow the conventions mapped out for the first set, but leave out the parts concerning parameters A and P: E15A:2Ds, for example, is progenitor E15A of Heger et al. (2000) evolved in axisymmetry, but with "shellular rotation." Table 1 lists the initial model parameters for E15A, E20A, and m15b6.

4. RESULTS

The focus of this study is on the periods and rotational profiles of the PNSs as obtained from our one-dimensional and two-dimensional radiation-hydrodynamics simulations. For more in-depth discussions of the supernova physics, we refer the reader to Thompson et al. (2005) for the one-dimensional simulations with SESAME and to Walder et al. (2005) for the two-dimensional MGFLD VULCAN/2D simulations.

Before we begin the discussion of our models, let us briefly summarize core collapse and bounce. Soon after the Chandrasekhar core begins to collapse, a subsonic, almost homologous ($v \propto r$) collapsing central region (the inner core) forms, while the outer core collapses supersonically. With increasing density, electron capture rates grow and at roughly 10^{12} g cm^{-3} the matter becomes opaque to electron neutrinos, which are then "trapped" in the core. As nuclear density is approached, nuclear repulsive forces lead to a sudden stiffening of the EOS. The inner core "bounces" and sends out an outgoing pressure wave which turns into the "bounce shock" when it reaches the sonic point at the interface between the homologously collapsing inner core and the supersonically collapsing outer core. The story of rotating core collapse is not greatly different. In addition to the interplay of gravity and pressure gradients one has to take into account the action of centrifugal forces. Because of angular momentum conservation during collapse, centrifugal support increases and leads to a somewhat later bounce and an oblate deformation of the collapsing core. Depending on the the total amount of angular momentum and its distribution throughout the iron core, the effects of rotation can be either minor, leading only to a slight oblateness of the core, or major, resulting in core bounce strongly affected by centrifugal forces at subnuclear densities (Ott et al. 2004; Zwerger & Müller 1997; Mönchmeyer et al. 1991). In rotating core collapse, an homologously collapsing inner core still forms, but, as pointed out by Zwerger & Müller (1997), the time-dependent proportionality factor α, relating the radial infall velocity v_r to the radius, also depends on the latitudinal angular coordinate Θ: $v_r = \alpha(t,\Theta)r$. α is largest close to the rotation axis and smallest on the equator where centrifugal support is strongest.

4.1. *One-dimensional Simulations*

In one spatial dimension, it is impossible to properly reproduce the rotational flattening of the collapsing iron core. If, however, the presupernova iron core rotates slowly (initial $\beta = T/|W| \lesssim 0.1\%$), the influence of centrifugal forces remains small during collapse and the oblate deformation of the core is almost negligible. In this case, the homologous collapse velocity of the inner core is roughly independent of Θ and the one-dimensional approximation for rotational core collapse is not bad.

An interesting consequence of the self-similar, homologous nature of the inner core's collapse in one dimension is the preservation of its initial rotational profile in the PNS from the precollapse state. In other words, if the inner core is initially rotating rigidly (which is likely to be the case; see Heger et al. 2000, 2005 and Fig. 1), then the inner PNS will be in solid-body rotation as well. This is nicely demonstrated by Fig. 3, which shows the evolution of the central angular velocity profile from the precollapse stage to the end of the supernova simulation for models s11A1000P4.00:1D and s11A1000P8.00:1D. Both models are initially forced to rotate with the same rotation law (see eq. 1), but with different initial central periods (separated by a factor of two, as is apparent from the model names). Due to angular momentum conservation and homologous collapse, the solid-body nature of the inner core's rotation is preserved during collapse and these PNSs are both rotating rigidly out to approximately 10 km or $0.5\ M_\odot$ in mass coordinate. In addition, the ratio between the two models' central periods remains approximately constant throughout the evolution. Note that material at or close to nuclear density can only very slowly contract on later cooling (Kelvin-Helmholtz) timescales. As a consequence, the central angular velocity of PNSs remains almost constant during the postbounce stage (unless angular momentum is redistributed by some agent, e.g. viscosity as we will discuss below).

There is a region in any PNS that is rotating differentially — independent of the angular momentum distribution in the progenitor core. Due to angular momentum conservation the core spins up during collapse. Since the inner parts of the precollapse iron core collapse to smaller radii than the supersonically collapsing outer parts, differential rotation is a natural consequence of collapse. However, solid-body rotation is the lowest-energy state of a rotating body and viscous processes can drive the differentially rotating PNS into rigid rotation as it evolves, cools and condenses to its final configuration. As Thompson et al. (2005) have pointed out, early and efficient postbounce dissipation of the shear energy stored in the differential rotation of the PNS by viscous processes (e.g., the MRI) can significantly affect the dynamics and might result in a successful explosion. To estimate the rotation periods our PNSs would have if they were in solid-body rotation, we introduce a moment of inertia-weighted mean angular velocity:

$$\bar{\Omega}(\zeta) = \frac{\int_{r=0}^{R} \zeta\rho(\mathbf{r})\Omega(\mathbf{r}) r_\perp^2 \, \mathrm{d}^3 r}{\int_{r=0}^{R} \zeta\rho(\mathbf{r}) r_\perp^2 \, \mathrm{d}^3 r}\,, \qquad (2)$$

where $r_\perp$ is the distance from the rotation axis at any given $\mathbf{r}$, $r = |\mathbf{r}|$ is the spherical radius, R is the outer radius of the computational domain and $\rho(r)$ is the matter density. In the one-dimensional case, r and $r_\perp$ are identical. We now define

two mean rotation periods. The definition of the function ζ depends on the individual mean being considered. The first mean period we define is

$$\bar{P}_{\rho 12} = 2\pi(\bar{\Omega}(\zeta))^{-1}\ \text{, where}$$
$$\zeta(\mathbf{r}) = \begin{cases} 1 & \text{if } \rho(\mathbf{r}) \geq 10^{12}\,\text{g cm}^{-3} \\ 0 & \text{otherwise} \end{cases} . \quad (3)$$

$\bar{P}_{\rho 12}$ is the period that all material with $\rho \geq 10^{12}$ g cm^{-3} would have if it were in solid-body rotation. We use this quantity to describe the postbounce spin evolution of the PNS. It is particularly useful because it captures the effects of accretion and contraction to higher densities and is meaningful in both one and two spatial dimensions. We adopt the density cut of 10^{12} g cm^{-3}, roughly marking the characteristic density at which neutrinos decouple from the fluid, to define the "edge" of the PNS for analysis purposes. Clearly, a PNS does not have a sharp boundary. However, most of its material has densities above the assumed density cut. The second mean period is

$$\bar{P}_{\rm M} = 2\pi(\bar{\Omega}(\zeta))^{-1}\ \text{, where}$$
$$\zeta(r, {\rm M}) = \begin{cases} 1 & \text{if } {\rm M}(r) \leq {\rm M} \\ 0 & \text{otherwise} \end{cases} . \quad (4)$$

$\bar{P}_{\rm M}$ is the period that the material interior to a given mass coordinate M would have if it were in solid-body rotation. An unambiguous definition of this quantity is only possible in one spatial dimension, because, in two dimensions one cannot assume that the matter distribution remains spherically symmetric — rotation and postbounce convection break spherical symmetry in any two-dimensional model.

The evolution of the postbounce mean period $\bar{P}_{\rho 12}$ as defined above is shown in Fig. 4 for a variety of models of the s11 model series. Shown in solid lines is the mean period for models without active viscous dissipation (:1D models). In dotted lines we plot the corresponding models in which we include viscous dissipation (:1Dv models). Let us first focus on the evolution of $\bar{P}_{\rho 12}$ for models without the inclusion of viscous effects. During collapse, $\bar{P}_{\rho 12}$ remains undefined until the density reaches the threshold value of 10^{12} g cm^{-3}. Initially it increases as more slowly rotating material achieves a density of 10^{12} g cm^{-3} and reaches its maximum just $\sim$1 ms before core bounce, when the lion's share of the inner core has crossed the density threshold, but has still not spun up to its bounce angular velocity. At bounce, $\bar{P}_{\rho 12}$ experiences a local minimum and then increases again as the core re-expands to a quasi-equilibrium configuration.

Model s11A1000P1.25:1D (shown in black in Fig. 4) is our fastest rotator, with an initial central period of 1.25 s and β = T/$|W|$ $\sim$0.9%. It undergoes a core bounce altered by centrifugal forces and forms a quickly spinning PNS with a central period of $\sim$1 ms. As displayed in Fig. 4, its mean period $\bar{P}_{\rho 12}$ stays almost constant at $\sim$3 ms until the end of the calculation. Because of strong centrifugal support, its protoneutron star is large and, even though matter is accreting, is only slowly contracting. Furthermore, model s11A1000P1.25:1D is the only one-dimensional model without viscous dissipation that exhibits an explosion — though a weak one — and less matter is accreted onto the PNS than in models that do not explode. Model s11A1000P2.00:1D is the next slowest rotator in our s11 model series. Its core bounce is dominated by nuclear repulsive forces, but centrifugal forces still play an important role. Its $\bar{P}_{\rho 12}$ increases slightly after bounce, reaches a local maximum at a time of $\sim$30 ms after bounce, and decreases from thereon to a final[3] $\bar{P}_{\rho 12}$ of 3.5 ms.

With increasing initial central rotation period, the influence of centrifugal forces becomes less and less relevant. As can be inferred from Table 2, the initial value of β is already as low as 0.25% for model s11A1000P3.00. In Fig. 4 all models with initial central period above 3 seconds show the same qualitative behavior: a short increase of $\bar{P}_{\rho 12}$ after bounce and then a monotonic decrease as more material is crossing the 10^{12} g cm^{-3} density threshold and piling up on the PNS. The slowest model evolved without viscous dissipation, s11A1000P10.47:1D, has a final ($\sim$500 ms after bounce) mean period of $\sim$14 ms. Model s11A∞P10.47:1D (magenta graph in Fig. 4) has a rotation parameter A (eq. [1]) set to infinity, forcing the initial model to rotate like a solid body. Compared with model s11A1000P10.47:1D, s11A∞P10.47:1D has significantly more angular momentum in the outer regions of the core. This difference has a major impact on the PNS's rotation and leads to a $\sim$50% smaller final mean period.

Dissipation of the shear energy stored in differential rotation is, as Thompson et al. (2005) report, most efficient in fast rotating models. This is supported by the evolution of our s11 models that include the effects of viscous energy dissipation and angular momentum redistribution after bounce. In Fig. 4, we plot in dotted lines the evolution of $\bar{P}_{\rho 12}$ for our :1Dv models. For model s11A1000P2.00, the :1Dv variant begins to deviate significantly from the model without viscous dissipation at about 40 ms after bounce. While the :1D model's mean period slightly decreases, $\bar{P}_{\rho 12}$ of the :1Dv model increases strongly as long as the angular momentum redistribution mechanism provided by viscosity remains efficient, that is, as long as there is considerable shear energy in differential rotation that can be dissipated and as long as the viscous timescale is short with respect to the Kelvin-Helmholtz timescale. Eventually, at $\sim$300 ms after bounce the entire PNS is in solid-body rotation and $\bar{P}_{\rho 12}$ remains constant, or decreases slightly, as the PNS contracts. All fast models for which we have performed :1Dv evolution (s11A1000P2.00, s11A1000P3.00, s11A1000P4.00) experience successful explosions (for details on the explosion mechanism, see Thompson et al. 2005). Since rotational energy scales with Ω^2, there is, for the same qualitative rotational profile, much less energy stored in the differential rotation of slow models than in fast models. This is why slow one-dimensional rotators ($P_0 \gtrsim 5$ s) do not explode even with the additional heating provided by viscous dissipation. Furthermore, this comports with the fact that the change in $\bar{P}_{\rho 12}$ brought about by the inclusion of viscous effects operating on differential rotation becomes smaller with increasing initial period. (Recall that the viscous timescale scales with Ω^{-1}; Thompson et al. 2005.)

The global ratio of rotational kinetic energy T to gravitational potential energy $|$W$|$, the rotation parameter β = T/$|$W$|$, is another useful and important quantity whose evolution we follow for all our models. If the value of β passes some critical threshold value, nonaxisymmetric rotational fluid instabilities may set in and lead to large-scale deformation of the core. In the approximation of MacLaurin spheroids (uniform

[3] In the following — unless otherwise stated — "final" means "at the end of the numerical evolution."

density, incompressible, rigidly rotating equilibrium configurations), triaxial instabilities may grow if $\beta \geq 14\%$ and $\beta \geq 27\%$ for secular and dynamical instabilities, respectively (Tassoul 1978). Given recent results by Ott et al. (2005) (see also Centrella et al. 2001; Shibata et al. 2002; Saijo et al. 2003; Shibata et al. 2003), it is likely that the above canonical threshold values for β do not hold for differentially rotating postbounce cores with a realistic equation of state. Ott et al. (2005) have found that a dynamical m = 1–dominated spiral instability may set in at a β as low as 8%. Nonaxisymmetric instabilities are of particular interest because they may lead to the emission of strong gravitational waves and to angular momentum redistribution and spindown of the central core.

Figure 5 shows the evolution of β for selected :1D and :1Dv models of the s11 model series. s11A1000P1.25:1D is the fastest rotator in this series. Initially, β is 0.88% for this model and it reaches a local maximum of 14.6% at bounce. After bounce, the relaxing core, abetted by centrifugal forces, overshoots its equilibrium configuration, leading to a pronounced local minimum in β of 12% about 3 ms after bounce [4]. Immediately following the initial postbounce relaxation, β begins to increase and does so throughout the rest of the evolution, reaching a β_f (the f indicating "final") of 18.4% at the end of our numerical evolution. Given the approximate constancy of the mean period $\bar{P}_{\rho 12}$ of model s11A1000P1.25:1D (Fig. 4) the above might seem surprising. However, β is a global quantity; the integrals for T and W encompass the entire grid and not just material above a density cut. Hence, the linear (in time) increase in global β indicates that the protoneutron star is slowly beginning to contract and spin up, but also that more and more material from larger radii is falling in, spinning up and settling onto the PNS surface. Both T and |W| increase, with T dominating, because of its higher-power dependence on the radial coordinate.

The β evolution for the rest of the s11 models without viscous dissipation is essentially the same as the one just described for model s11A1000P1.25:1D. With decreasing initial β, β at bounce and β_f decrease. Model s11A∞P10.47:1D, whose core is initially in solid-body rotation, stands out. Even though its initial period P_0 is the same as model s11A1000P10.47:1D's, its initial value of β is more than four times larger (see Table 2) than s11A1000P10.47:1D's. As shown in Fig. 5, this is reflected in its β evolution up to bounce and, most apparently, in the steeper increase in the postbounce phase.

Two of our models from the s11 model series, namely s11A1000P1.25:1D and s11A1000P2.00:1D surpass β = 8% during their numerical evolution. They also exhibit strong differential rotation (Fig. 6) and might experience the m=1-dominated one-armed spiral instability (Ott et al. 2005). s11A1000P1.25:1D even reaches $\beta \geq 14\%$ and may become unstable towards a "classical" bar-like instability on a secular timescale.

The evolution of β for models with viscous angular momentum redistribution is quite different (Fig. 5). As soon as the viscous terms are switched on after bounce (§2.1), for :1Dv models with $P_0 \lesssim 4$ s (red, green and brown dotted lines in Fig. 5) β begins to decrease. Shear energy stored in the differential rotation of the PNS is dissipated away, leading to solid-body rotation at lower angular velocities and, hence, lower rotational kinetic energies. As discussed by Thompson et al. (2005), models s11A1000P2.00:1Dv and s11A1000P3.00:1Dv experience energetic explosions that remove a significant fraction of the stellar envelope. Therefore the PNS masses remain somewhat smaller than for s11A1000P4.00:1Dv, which explodes less energetically and at later times, allowing more matter to accrete through the stalled supernova shock and onto the PNS (Fig. 7). In model s11A1000P4.00:1Dv, β decreases for the first 100 ms and then increases again. This is, in part, because of the $\sim \Omega^3$ dependence of the viscous dissipation and, in part, because of its weak and later explosion that results in more mass being accreted than in the two faster models discussed. For even slower models, the evolution of β is similar to those for the cases without viscosity. Model s11A∞P10.47:1Dv departs from the :1D evolution at late times when high-angular momentum material reaches small radii and the energy stored in differential rotation becomes large. Viscous dissipation of that energy then leads to a smaller final β than in the :1D model without viscous dissipation.

In Fig. 6, we present the final period (Fig. 6a) and angular velocity profiles (Fig. 6b) of a representative subset of the s11 model series calculated with SESAME. Profiles of models with viscous dissipation and angular momentum redistribution are drawn as dotted lines, profiles of models without viscous effects are drawn as solid lines. Model s11A1000P1.25:1D, drawn in black, has the shortest initial central period (P_0 = 1.25 s) which maps to the shortest final central period of $P_{0,f}$ = 1.56 ms. As discussed earlier in this section, the PNSs are in solid-body rotation inside 8 – 10 km (or $\sim$0.5 – 0.8 $M_\odot$ in mass coordinate). At greater radii, the PNSs quickly become differentially rotating. For model s11A1000P1.25:1D, the angular velocity drops from $\sim$2500 rad s^{-1} at 20 km to $\sim$900 rad s^{-1} at 50 km and $\sim$330 rad s^{-1} at 100 km, corresponding to a $\Delta\Omega/\Delta r$ of 53 rad s^{-1} km^{-1} from 20 to 50 km and 11 rad s^{-1} km^{-1} from 50 to 100 km (be aware of the log-log scale in Fig. 6). Again, one has to keep in mind that model s11A1000P1.25:1D explodes. The explosion removes material that would otherwise accrete onto the PNS and pile up on the quasi-incompressible inner region above radii of 15 – 30 km. This is reflected in the features visible in the graphs of :1D models with $P_0 \geq 2$ s in the range of radii mentioned. Models in which we include viscous dissipation and angular momentum transport exhibit solid-body rotation out to much larger radii. Model s11A1000P2.00:1Dv, for example, rotates rigidly out to $\sim$23 km or 0.9 $M_\odot$ in mass coordinate while model s11A1000P2.00:1D exhibits solid-body rotation out to only $\sim$10 km or 0.42 $M_\odot$[5]. Viscous dissipation of shear energy stored in differential rotation also leads to a spindown of the PNS. s11A1000P2.00:1D's final central period is 1.95 ms whereas s11A1000P2.00:1Dv spins with a final central period of 6.7 ms, which is more than 3.5 times slower. Due to the Ω^2 dependence of rotational energy and the Ω^3 dependence of the dissipation rate, the relative period increase brought about by viscous dissipation/angular momentum transport decreases quickly with increasing P_0. For s11A1000P3.00 (central periods: 2.74 ms and 6.16 ms for the :1D and :1Dv models, respectively), the ratio is down to about 2.2 and for s11A1000P10.47 (central periods of 9.19 ms and 16.0 ms for

[4] Due to the range in time we are showing in Fig. 5, this local minimum is not clearly visible.

[5] See Fig. 7b for the mapping between mass and radial coordinates at the end of each model's numerical evolution.

models :1D and :1Dv, respectively), it is approximately 1.7. Of course, the just quoted ratios depend on the simulation time after bounce, which determines how much time we have allowed the dissipative process to spin down the core and how much material and angular momentum is accreted during the simulation. Model s11A∞P10.47 stands out. It contains significantly more angular momentum than its counterpart with A = 1000 km. Therefore, it spins up to shorter central periods during collapse and during the postbounce evolution.

For key models of the s11 model series, the final moment-of-inertia-weighted mean period $\bar{P}_M$, as defined by eq. (4), is shown in Fig. 7a. Note that $\bar{P}_M$ gives the mean period of material inside a mass coordinate M, assuming solid-body rotation. Hence, the graphs should not be interpreted as profiles in the usual sense. The mass coordinate at which the slope of each individual model's $\bar{P}_M$ sharply steepens is a good estimate for the compact remnant mass in models that exhibit explosions. s11A1000P2.00:1Dv (dotted red), for example, explodes early and energetically, leaving behind a lower-mass PNS than model s11A1000P3.00:1Dv (dotted green), which explodes at a somewhat later time. For models that don't explode, $\bar{P}_M$ jumps only at $\sim$1.42 $M_\odot$. The consequences of viscous dissipation and angular momentum redistribution in the :1Dv models, spindown and solid-body rotation, are perhaps even more obvious in Fig. 7a than in Fig. 6. Also, note that, since the :1Dv models are in solid-body rotation throughout most of the protoneutron star at the end of our calculations, $\bar{P}_M$ for them agrees very well with the actual period profiles.

Aside from initial central period and the initial angular velocity profile, a third important input parameter, the progenitor star structure, determines the spin of a nascent neutron star. In order to gauge the impact of progenitor structure on the spin rates and rotational profiles of protoneutron stars, we have performed a set of calculations in spherical symmetry with SESAME employing the s15, s20 (15 $M_\odot$ and 20 $M_\odot$ at ZAMS, respectively) progenitors of Woosley & Weaver (1995), the E15A and E20A presupernova models of Heger et al. (2000), and the m15b6 progenitor of Heger et al. (2005). The key progenitor characteristics of all models are summarized in Table 1. In the following we present the results of these calculations and compare them with those of our s11 models.

In Fig. 8, we display the evolution of the angular velocity profiles for models s11A1000P2.34, s15A1000P2.34, s20A1000P2.34, E15A, E20A and m15b6 in their :1D and :1Dv variants. The latter three models' progenitors are rotating, that is, they were evolved in spherical symmetry until the onset of core collapse with a one-dimensional prescription for the treatment of rotation. Hence, we do not have to artificially force them into rotation by the rotation law of eq. (1). The former three models were set into rotation, using identical values for A and P_0 in order to separate out the effect of different progenitor structure. We choose P_0 = 2.34 s and A = 1000 km to facilitate the comparison (§5) with our two-dimensional models.

The evolution of the angular velocity profile from the initial profile to bounce and during the postbounce stages of models s11A1000P2.34:1D (solid lines) and :1Dv (dotted lines) is shown in panel (a) of Fig. 8. Due to SESAME's Lagrangean nature, the first data point of the models' initial Ω profile (red) is at $\sim$25 km. At bounce (drawn in black), the central Ω reaches $\sim$2800 rad s^{-1} and stays roughly constant out to 15 km. In the :1D model, the Ω profile at bounce is preserved approximately until the end of the evolution. Due to the quasi-incompressibility of the inner PNS, the central regions spin up only slightly, while higher specific angular momentum material is piling up onto the PNS at larger radii. This is most clearly visible in the mildly positive slope of $\Omega(r)$ inside $\sim$10 km, which develops soon after bounce, and also in the "bump" at $\sim$35 km in the final profile (solid magenta). The postbounce evolution of the :1Dv model (dotted lines) is radically different. Due to the dissipation of shear energy stored in differential rotation and angular momentum redistribution, the PNS has already spun down to 1900 rad s^{-1} in the center only 50 ms after bounce (yellow dotted). Another 100 ms later (blue dotted), the central Ω is down to 1250 rad s^{-1} and a significant amount of angular momentum has been transported out to larger radii, leading to higher angular velocities there. At 300 ms (green dotted) after bounce, most of the shear energy has been dissipated and a successful explosion has been launched in the :1Dv model. The protoneutron star is rotating like a solid body out to about 30 km. The final (in the :1Dv model, 437 ms after bounce) central Ω is 915 rad s^{-1}, corresponding to a final central period of 6.9 ms, and the PNS is in solid-body rotation out to about 40 km. For comparison, the final central angular velocity of the :1D model is 2860 rad s^{-1}, corresponding to a central spin period of 2.2 ms.

Surprisingly similar to their s11 counterparts are the spin histories of models s15A1000P2.34:1D and s15A1000P2.34:1Dv, portrayed in panel (b) of Fig. 8. This similarity is explained by the virtually identical progenitor structure of s11 and s15 (out to 1000 km; see Fig. 2). Only at late times, when outer core material reaches small radii, does the s15A1000P2.34:1D profile exhibit slightly larger Ωs at intermediate radii than does that of s11A1000P2.34:1D. The spin profiles of s11A1000P2.34:1Dv and s151000P2.34:1Dv remain practically unchanged to late times, since their successful explosions remove the outer core material.

With models s20A1000P2.34:1D and :1Dv (displayed in panel c of Fig. 8) one again notices the qualitative similarity with the corresponding s11 and s15 models discussed above. However, the Woosley & Weaver (1995) s20 presupernova model, as displayed in Fig. 2, has a significantly larger and more massive core and a shallower density stratification than both s11 and s15. Even though we set up rotation in s20A1000P2.34 in the same way we do with s11/s15A1000P2.34, the former model reaches a central Ω at bounce of 5200 rad s^{-1} which is almost twice as high as the corresponding values for s11A1000P2.34 and s15A1000P2.34. This is entirely due to the much shallower density profile of the s20 presupernova model (see Fig. 2). Because of the lower initial density inside the inner presupernova core (out to $\sim$500 km), the core material compresses more (in density and radius) and, hence, reaches higher angular velocities. It is remarkable, but not surprising, that viscous dissipation/angular momentum redistribution is able to spin the PNS down to a central angular velocity of just below 1000 rad s^{-1} — a value that is very close to the final central angular velocities of both s11A1000P2.34:1Dv and s15A1000P2.34:1Dv.

The presupernova model E15A of Heger et al. (2000) was evolved in spherical symmetry with the inclusion of rotation. In Fig. 1b, we plot (in magenta) E15A's initial angular velocity profile. Its initial central Ω is 4.18 rad s^{-1}, which corresponds to P_0 = 1.5 s. Apparent in Fig. 1 are the dis-

continuities in the rotational profiles of the rotating progenitors E15A, E20A, and m15b6. These correspond to compositional interfaces, which in turn are a result of discrete convective nuclear burning shells in the progenitor star. The short convective timescale leads to roughly constant angular velocity in these regions and shear viscosity is not believed to smooth out the discontinuities in the rotational profile during stellar evolution (Heger et al. 2000). In panel (d) of Fig. 8, we show the evolution of the angular velocity profile of models E15A:1D and E15A:1Dv. The most apparent qualitative difference with the Woosley & Weaver (1995) models are the clearly visible discontinuities in the angular velocity profiles that are preserved during collapse and in the postbounce phase of model E15A:1D, but smoothed out in the postbounce evolution of E15A:1Dv. In comparison with s15A1000P2.34:1D, E15A:1D reaches a higher central Ω of $\sim$4900 rad s^{-1}. This is due to its shorter initial spin period and its shallower density profile compared with model s15A1000P2.34 (or s11A1000P2.34). E15A:1D and E15A:1Dv are, in fact, more similar to s20A1000P2.34:1D and :1Dv. Again, in E15A's :1Dv variant, solid-body rotation at lower angular velocity is enforced by viscous dissipation and angular momentum transport. At the end of the simulation, E15A:1Dv is in solid-body rotation out to about 32 km with an angular velocity of $\sim$1085 rad s^{-1}, which corresponds to a spin period of 5.8 ms.

The spins of models E20A:1D and E20A:1Dv (panel (e) of Fig. 8) evolve in a manner qualitatively similar to models E15A:1D and E15A:1Dv. The differences in their initial density stratifications are small enough (Fig. 2) for the quantitative differences in their Ω histories to be caused predominantly by the initially slower overall rotation of E20A (Fig. 1). Since E20A's central core is slightly more extended than E15A's, its region of solid-body rotation in both the :1D and :1Dv variants is larger. Furthermore, note that not all :1D models explode. Models s11A1000P2.34:1Dv, s15A1000P2.34:1Dv, and E15A:1Dv explode successfully before the end of our calculations. However, models s20A1000P2.34:1Dv and E20A:1Dv do not explode before we end the simulations, though they both exhibit slowly outward moving shocks, perhaps presaging a late explosion.

Panel (f) of Fig. 8 shows the evolution of the Ω profiles of models m15b6:1D and m15b6:1Dv. The progenitor star model m15b6 is drawn from the study of Heger et al. (2005) and was evolved with rotation and angular momentum redistribution by magnetic torques. Its initial central period is 31.73 s - more than an order of magnitude larger than the initial periods of the other models presented in Fig. 8. Models m15b6:1D and m15b6:1Dv yield no qualitative surprises. m15b6's inner core collapses to smaller radii than, for example, s15A100P2.34's, since centrifugal support is significantly weaker in the former. As stated, the mechanism for viscous dissipation that we consider is most efficient in quickly spinning PNSs. Hence, the relative decrease in Ω is smaller in m15b6:1Dv than in other :1Dv models, but still significant. At bounce, m15b6's central angular velocity is 220 rad s^{-1}. The final central Ω in variant :1Dv is $\sim$135 rad s^{-1}, corresponding to a period of 46.5 ms. In the :1D variant, the final central angular velocity is slightly up from the bounce value at 226 rad s^{-1} which corresponds to a central period of 27.8 ms. The final mean periods ($\bar{P}_{\rho 12}$) of the two m15b6 variants do not differ appreciably.

In Fig. 9, we show the postbounce evolution of the moment-of-inertia-weighted mean period $\bar{P}_{\rho 12}$ for models with different presupernova structure. Note that the range of $\bar{P}_{\rho 12}$ which we plot is much smaller than in Fig. 4, since we are focussing on fast models with final $\bar{P}_{\rho 12}$ below $\sim$8 ms. The small periodic jumps in $\bar{P}_{\rho 12}$ are artefacts introduced by individual Lagrangean mass zones moving above and/or below the density threshold of 10^{12} g cm^{-3}. Models s11A1000P1.25 and E15A have the shortest initial central periods of all models in our study, 1.25 s and 1.5 s, respectively. Despite the differences in their progenitor stellar structure and rotational profile (Fig. 1), their :1D variants' $\bar{P}_{\rho 12}$ evolution is qualitatively very similar, only offset due to the difference in their initial periods. However, at late times E15A:1D's more massive, initially lower-density core leads to lower $\bar{P}_{\rho 12}$, reaching 2.91 ms at the end of the simulation. s11A1000P1.25:1D's $\bar{P}_{\rho 12}$ also exhibits a non-zero negative, though smaller in magnitude, slope at the end of its numerical evolution. Since this model explodes, the changes in $\bar{P}_{\rho 12}$ are related to the slow contraction and accretion of the remaining material.

As expected, the mean periods of s11A1000P2.34:1D(v) and s15A1000P2.34:1D(v) are qualitatively and quantitatively very similar: at the end of these simulations 3.85 ms and 3.95 ms, for s11A1000P2.34:1D and s15A1000P2.34:1D, respectively. The :1Dv models' $\bar{P}_{\rho 12}$ evolutions begin to depart significantly from the :1D models' shortly after bounce, increasing strongly until a maximum at a time of $\sim$200 ms after bounce is reached. At that point, most of the PNS has already been brought into solid-body rotation by the action of viscous angular momentum redistribution. The further evolution of $\bar{P}_{\rho 12}$ in the :1Dv models is then dominated by PNS cooling and compression of post-shock material onto the PNS, leading to a decrease in $\bar{P}_{\rho 12}$. For example, at 150 ms after bounce, 1.0 M$_\odot$ of s11A1000P2.34:1Dv has densities $\rho \geq 10^{12}$ g cm^{-3}, whereas at the end of this model's evolution, almost 1.2 M$_\odot$ has densities above that threshold. Models s11A1000P2.34:1Dv and s15A1000P2.34:1Dv reach final mean periods of 7.18 ms and 6.76 ms, respectively.

Model s20A1000P2.34:1D, despite having the same initial angular velocity profile, shows a $\bar{P}_{\rho 12}$ evolution that is quite different from those of s11/s15A1000P2.34:1D. As pointed out in the discussion on Fig. 8, this is due to the considerably more massive and extended iron core of the s20 progenitor. Right after bounce, this model's $\bar{P}_{\rho 12}$ is almost a factor of two smaller than s15A1000P2.34:1D's $\bar{P}_{\rho 12}$. It then increases until about 80 ms after bounce and then begins to decrease again. Its final $\bar{P}_{\rho 12}$ is 3.48 ms. This behavior can be explained as follows. In the early postbounce evolution the PNS is still extended and material that is crossing the $\bar{P}_{\rho 12}$ density threshold stays at relatively large radii, not spinning up dramatically. $\bar{P}_{\rho 12}$ increases. Eventually the PNS contracts as more material is accreted. Material that was previously at larger radii is pushed to smaller radii, thus spinning up the core and decreasing $\bar{P}_{\rho 12}$. This argument can equally well be applied to the $\bar{P}_{\rho 12}$ evolution of E20A:1D, which reaches a $\bar{P}_{\rho 12}$ of 3.43 ms at the end of the calculation. Viscous dissipation and angular momentum redistribution are very efficient in s20A1000P2.34:1Dv and E20A:1Dv. The final $\bar{P}_{\rho 12}$ s are 6.8 ms and 6.9 ms, respectively. It is interesting to note that the final mean periods of all the :1D variants fall into the relatively narrow range of 3 to 4.5 ms, while the final mean periods of the :1Dv variants all fall into an even narrower range

of 6 to 7 ms.

Figure 10 compares the histories of the rotation parameter β = T/|W| for the same set of models. The overall characteristics are the same as detailed previously for $\bar{P}_{\rho 12}$ and for the individual angular velocity profiles displayed in Fig. 8; s20A1000P2.34, E20A, E15A spin up to higher β than the slower and/or less massive models. The β evolution of models s11A1000P2.34 and s15A1000P2.34 is very similar. Interestingly, the β evolution of model E20A:1D deviates from the standard picture. Its postbounce increase is much smaller than that of models E15A:1D or s20A1000P2.34:1D. We attribute this difference to the postbounce interplay of E20A's larger core and, hence, larger gravitational binding energy (|W|), with the lower specific angular momentum in its accreting outer core region, leading to a slower increase of rotational kinetic energy (T) than in the other models [6].

At the end of our calculations, all :1D variants presented in Fig. 10 have $\beta \geq 8\%$ and exhibit considerable differential rotation outside $r \sim 15$ km (Fig. 8). They might be susceptible to the m=1-dominated one-armed spiral instability discussed by Ott et al. (2005). Models s11A1000P1.25:1D, E15A:1D, and s20A1000P2.34:1D even reach $\beta \geq 14\%$ and may become unstable to the more canonical secular bar-mode instability. The β evolution of the :1Dv variants is different. Viscous dissipation and angular momentum redistribution lead to sharply dropping β as soon as the viscous terms are switched on. The final β of all :1Dv variants is between 2% and 5%. Furthermore, these models are in solid-body rotation throughout the PNS and nonaxisymmetric instabilities are not likely to arise. Again, E20A stands out. Its :1Dv variant's β first decreases after bounce, but then, after $\sim$200 ms, increases again. To understand this, it is useful to consider the angular velocity profiles in Fig. 8e (dotted lines for E20A:1Dv). In this :1Dv model, material at large radii is spun up while the PNS angular velocity stays practically constant at late times. (Fig. 8; see also Fig. 1). This leads to the observed late time increase in β.

4.2. *2D Simulations*

We now discuss the results of the axisymmetric 2D VULCAN simulations using the methods described in §2.2. In contrast to the spherically symmetric simulations, two-dimensional, azimuthally-symmetric simulations are able to follow the non-spherical effects of rotation in core collapse. The degree of oblate deformation can be described by the ratio of the PNS's polar and equatorial radii on isodensity surfaces, the so-called axis ratio. Figure 11 displays snapshots of the density at $\sim$200 ms after bounce for a set of representative 2D models. Models s11A1000P2.34 and E15A are the fastest rotators, having axis ratios below 1:2. Clearly, a two-dimensional treatment is a must for capturing the full dynamics of these rapid rotators. With increasing initial iron core period (P_0) the PNS axis ratio increases towards one. m15b6 and the two variants of s11A1000P10.47:2D exhibit almost no rotational flattening at all and one might expect a one-dimensional treatment to yield good results. But it is not only rotation that is modeled much more realistically in real 2D simulations. Neutrino-driven convection naturally develops in the region behind the stalled supernova shock and leads to the interesting substructure seen in Fig. 11. The purely hydrodynamic model, s11A1000P10.47:2Dh, experiences a prompt explosion and Fig. 11 does not show the imprint of the vigorous convection present in the models that are evolved with adequate neutrino treatment and radiative transfer. Note that the small dents and spikes visible along the rotation axis in most of the panels are related to the imperfect symmetry axis treatment in the version of VULCAN/2D with which most of our models are evolved. The purely hydrodynamic model has been evolved with an updated version of the code and exhibits minimal axis artefacts.

Because of the computational difficulties that accompany long-term, two-dimensional radiation-hydrodynamics evolutions, we have run our two-dimensional models to postbounce times of only 200 – 300 ms and display profiles and two-dimensional snapshots at 200 ms after bounce. At that epoch, the PNS has already reached a compact state and the largest fraction of its final mass has already settled inside a (spherical) radius of $\sim$50 km. Figure 12 shows the mass contained inside a given spherical radius for selected models at 200 ms after core bounce. The graphs certainly ignore the two-dimensional nature of the calculation, but give a good (and for the slow models, almost accurate) handle on the mass-radius relationship. The dashed lines in Fig. 12 represent mass profiles of models that are evolved adiabatically and exhibit prompt explosions, blasting away a large fraction of the outer iron core and the stellar envelope. Hence, their PNS masses are small compared with those of the MGFLD models that might (or might not) explode at later times after much of the outer core has accreted onto the PNS. Note that slower models have more compact PNSs than faster models. This is, of course, expected since rotational support is greater in faster models and leads to more expanded postbounce configurations.

In Fig. 13, we depict the equatorial angular velocity and period profiles (panels (a) and (b), respectively) at 200 ms after bounce for the two-dimensional s11A1000 model series. For comparison we also display graphs of model s11A∞P10.47:2D (magenta; initially in solid-body rotation) and of two purely hydrodynamic models (dashed graphs). Note that the graphs start at a radius of 3 km to excise axis artefacts. The aim of Fig. 13 is to display the systematic dependence of the protoneutron star rotational profile on the initial iron core spin rate. For this, we focus in Fig. 13 on the angular velocity and period profiles of the MGFLD models s11A1000P157.10:2D, s11A1000P41.69:2D, s11A1000P10.47:2D, s11A1000P4.69:2D, and s11A1000P2.34:2D. These models form a sequence in initial rotation period from 157.10 s down to 2.34 s. At 200 ms after bounce, s11A1000P157.10:2D has reached a central period of $\sim$50 ms. The spin period increases by about a factor of two in going from 3 km to 5 km and then stays roughly constant, but shows significant substructure, out to 30 km. From 30 km to 100 km, the period increases by a factor of ten, corresponding to a "period slope" of $\sim$30 ms km^{-1}. We call the reader's attention to the region of quasi solid-body rotation between roughly 5 and 30 km also present in all spherically symmetric models (see §4.1 and Figs. 3, 6, and 8). This region is a direct consequence of self-similar collapse of the inner core. The equatorial angular velocity and period profiles of the two-dimensional models are, however, much less smooth than the profiles of the one-dimensional models (see Fig. 8). This is attributed to the much more complicated,

[6] Note the drop in Ω at $\sim$1000 km, visible in Fig. 1.

two-dimensional dynamics that involve convection and inviscid angular momentum redistribution along the rotation axis due to convection (Fig. 14). The hump in the angular velocity profile (corresponding to a notable dent in the period profile) at about 20 km is a generic feature in the entire s11A1000 series, but is most pronounced in the slow models. It is caused by accreting relatively high-specific angular momentum material that is piling up on the nuclear-density region of the PNS. The faster a model is, the more extended its PNS (see Fig. 12) and the shallower its density profile.

The qualitative shape of the angular velocity and period profiles of s11A1000P157.10:2D is mirrored, but of course shifted, in the Ωs (and periods) in faster models (Fig. 13). However, the profiles of faster models are smoother. Convection in fast models is largely suppressed by rotation in the equatorial regions [7] (Fryer & Heger 2000; Fryer & Warren 2004; Walder et al. 2005) and, hence, does not create as much substructure in the equatorial profiles as in slower models. In Fig. 13, for models s11A1000P2.34:2D and s11A1000P10.47:2D, we include equatorial profiles of their purely hydrodynamic :2Dh variants. They are plotted with dashed lines. Since we do not include any neutrino physics and transport in the :2Dh simulations, these models cannot contract and spin up to higher Ω after core bounce. They experience prompt explosions and fall-back accretion is negligible. Keeping this in mind, it is a bit surprising to see how similar the hydrodynamic models' profiles are to the profiles of their MGFLD counterparts. To conclude our discussion of Fig. 13, we call attention to the graphs of s11A∞P10.47:2D's angular velocity and period profile (magenta lines). This model is set up in solid-body rotation with an initial spin period of 10.47 s. Initial solid-body rotation means that a great part of the iron core's angular momentum is located at large radii (the r^2 moment arm balances the density drop with increasing radius). Due to angular momentum conservation during collapse, one expects the outer core layers to spin up appreciably. This is exactly what we see in Fig. 13: The region of high angular velocity ($\sim$600 rad s^{-1}) and low period ($\sim$10 ms) extends out to about 70 km, whereas s11A1000P10.47:2D's angular velocity (orange lines) starts dropping (and its period starts increasing) already at about 20 km. Note that the centermost regions of the two models agree relatively well — as they should — given the fact that s11A1000P10.47:2D's initial angular velocity is almost constant throughout its inner core (Fig. 1).

The fastest model of the series presented in Fig. 13 is s11A1000P2.34:2D. Its initial central iron core spin (P_0) of 2.34 s maps to a central postbounce period (at the 200 ms snapshot shown here) of about 1.7 ms, which increases to $\sim$3.2 ms at 10 km. As shown in Fig. 11, its PNS is rotationally flattened with an axes ratio below 1:2. In Fig. 14, we show the angular velocity distribution in s11A1000 models with P_0s of 2.34 s, 4.69 s, 10.47 s, and 41.89 s at 200 ms after bounce. Since we are imposing axisymmetry, the angular velocity distribution is symmetric with respect to the vertical axis (the rotation axis). We superpose flow velocity vectors to convey qualitatively the flow dynamics in the PNS. We downsample the number of velocity vectors at radii that are greater than the approximate shock location of each individual model. For the purely hydrodynamic model, the radius beyond which we downsample is chosen to be 150 km. The panels show the inner 400 km of the computational domain. (For a more detailed discussion of the multi-dimensional flow dynamics and its consequences concerning the supernova mechanism, we refer the reader to Walder et al. (2005).) All 2D models shown rotate in the precollapse stage with constant angular velocity on cylindrical shells. As the collapse proceeds, the matter falls in almost spherically (more spherically for slowly spinning models, less spherically for fast spinning models). The initial conditions and the collapse dynamics are reflected in the elongated (prolate) shape of the angular velocity distribution of the PNSs. The fast models (s11A1000P2.34:2D and s11A1000P4.69:2D) have a notable central spheroidal bulge of high angular velocity material, which is formed by high specific angular momentum material from the equatorial regions.

As in the discussion of our one-dimensional models in §4.1, we define a mean, moment-of-inertia-weighted period $\bar{P}_{\rho 12}$ for all material with density above 10^{12} g cm^{-3} (eqs. 2 and 3). Figure 15 depicts $\bar{P}_{\rho 12}$ as a function of time for all two-dimensional s11 models. In addition to the s11A1000 MGFLD models, we plot $\bar{P}_{\rho 12}$ for s11A∞P10.47:2D (magenta) and the purely hydrodynamic variants s11A1000P2.34:2Dh and s11A1000P10.47:2Dh (dashed lines). As one would expect, all models exhibit a local minimum of $\bar{P}_{\rho 12}$ at the time of core bounce. For the purely hydrodynamic models, this is the absolute minimum in $\bar{P}_{\rho 12}$, since they quickly achieve hydrostatic equilibrium after bounce. Their periods remain almost constant at postbounce times. Model s11A1000P2.34:2Dh (dashed red) undergoes core bounce aided by centrifugal forces and shows the pronounced postbounce coherent expansion and recontraction cycles described for these sorts of models in Ott et al. (2004). In contrast, s11A1000P2.34:2D, its MGFLD variant, relaxes from its local minimum in $\bar{P}_{\rho 12}$ and shows no oscillatory behavior at all. We attribute this major difference to the following phenomenon. In adiabatic collapse, angular momentum conservation during collapse leads to an increase in the kinetic energy stored in rotation. By its nature rotation acts approximately like a gas with Γ of 5/3 (Tassoul 1978; Mönchmeyer et al. 1991) and in this way effectively increases the pressure support of the collapsing core. At the moment of strongest compression at bounce, centrifugal forces are maximal and result in the core dramatically overshooting its postbounce equilibrium position. Recontraction follows, leading to another expansion-recontraction-bounce cycle. Eventually, enough pulsational energy is dissipated by the generation of secondary shocks that after several cycles the oscillation is damped. However, including the production and radiative transfer of neutrinos, the rebounding core loses a large amount of energy in the neutrino burst that occurs when the bounce shock wave breaks through the electron neutrinosphere. This, and continuing neutrino loses, lead to enhanced damping of the postbounce expansion-recontraction-bounce cycles, far more than experienced in quickly spinning purely hydrodynamic models.

We note that the qualitative shape for a given progenitor structure and rotational "scale height" A of the $\bar{P}_{\rho 12}$ evolution shown in Fig. 15 is the same for all s11A1000 models. Generally, at any postbounce time $\bar{P}_{\rho 12}$ is a monotonic

[7] Note, however, that for convection to be stabilized, the rotation rate must be large enough that if the calculation had been done in magneto-hydrodynamics, the region would likely be destabilized by the MRI (Thompson et al. 2005). We therefore expect that when these rapidly rotating models are calculated in MHD, they will show enhanced (magneto-)convection with respect to the hydrodynamical, centrifugally-stabilized calculations presented here.

function of the initial iron core spin. At 200 ms after core bounce, the largest $\bar{P}_{\rho 12}$ is $\sim$180 ms (s11A1000P157.10:2D) and the smallest is $\sim$4.7 ms (s11A1000P2.34:2D). In Table 3, we list the mean periods for all models at the end of their numerical runs. The magenta graph in Fig. 15 represents s11A∞P10.47:2D's $\bar{P}_{\rho 12}$ evolution. As expected, this initially rigidly rotating model's PNS is spinning faster than its counterpart with A set to 1000 km before collapse.

As demonstrated for the s11 model series in Fig. 16, the systematics with the global rotation parameter β is similar. Up to bounce, β increases monotonically in all models. The faster of the two purely hydrodynamic models (dotted-line graphs) reaches the highest β at bounce of all models presented in Fig. 16. Due to its higher electron fraction Y_e and higher effective adiabatic Γ (Martinez-Pinedo et al. 2004), in direct contrast with the more realistic MGFLD variant, s11A1000P2.34:2D, the purely hydrodynamic model has a much more massive inner core. Hence, during its "plunge" phase just before and at bounce, more material, and in that way more angular momentum, reaches small radii. This is why purely hydrodynamic models reach higher βs at bounce than their MGFLD diffusion counterparts. While the purely hydrodynamic models settle at a practically constant final β, all MGFLD models exhibit a linear postbounce growth of the rotation parameter, with a slope that depends on the initial iron core spin and on the scale parameter A in the rotation law. The increase in β is caused by the increase in compactness and by accretion of outer-core material. One might expect that the slope of β will change after a successful explosion (not tracked in our models). At the end of their numerical evolution none of the models presented in Fig. 16 has reached the classical threshold values of β for secular or dynamical instability. However, as Ott et al. (2005) have demonstrated, at $\beta \sim$8% realistic postbounce cores might undergo the low-T/|W| instability. This value is likely to be reached by model s11A1000P2.34:2D at late times.

Having described the quantitative and qualitative features of a neutron star's birth spin and its dependence on the initial iron core spin rate for a fixed progenitor structure, we now investigate the effect of varying progenitors on the PNS spin. In Fig. 17, we contrast the two-dimensional angular velocity distributions of models with different progenitor iron core mass and structure at $\sim$200 ms after core bounce. We zoom in on the inner 400 km of our computational domain. The rotation law parameters P_0 and A are prescribed. The top right panel of Fig. 17 shows an Ω snapshot of model s11A1000P2.34:2Dh, the purely hydrodynamic variant of s11A1000P2.34:2D. At $\sim$200 ms after bounce, this model has already undergone a prompt explosion. This explains the outward pointing fluid velocity vectors in this panel. The region of high angular velocity is stretched out along the axis of rotation (the vertical). This is caused by the prompt explosion, which leads to an ejection along the axis of high-Ω material from deep within the inner core.

The lower two panels of Fig. 17 show angular velocity distributions of models s15A1000P2.34:2D and s20A1000P2.34:2D, respectively. Comparing them to the top-left panel which shows model s11A1000P2.34:2D, one notes that the PNS rotational structure is not strongly dependent on progenitor mass; the three models in question have qualitatively and quantitatively very similar angular velocity distributions at 200 ms after bounce. For the s11 and s15 models, this is not surprising, given that their iron core masses and density profiles (Fig. 2 and Table 1) are very similar to each other. However, the s20 progenitor model which we use in our model s20A1000P2.34:2D has an appreciably different initial iron core structure. It is more extended, has a lower initial central density, and is significantly more massive than the s11 and s15 models. Yet, at 200 ms after bounce only small differences in the angular velocity distribution are apparent. s20A1000P2.34:2D's PNS is more massive and more extended. This is reflected in the slightly larger central spheroidal bulge of high-angular velocity material. As can be inferred from the flow patterns in Fig. 17, the thermodynamic structure and the resulting fluid dynamics of models s11A1000P2.34:2D, s15A1000P2.34:2D, and s20A1000P.23:2D are significantly different. These differences are reflected in the angular velocity distribution to only a slight degree.

Figure 18 depicts the angular velocity distributions of the recent rotating "Heger models" (Heger et al. 2000; Heger et al. 2005) at 200 ms after core bounce. We include models E15A, E20A, and m15b6 in our two-dimensional model set and for model E15A:2D also perform a simulation with initial "shellular rotation" (E15A:2Ds; see §3). The upper left and upper right panels of Fig. 18 are snapshots of the two-dimensional Ω distributions of models E15A:2D and E15A:2Ds, respectively. One can easily discern the more sphere-like Ω distribution of E15A:2Ds at large radii. E15A:2Ds' angular velocity in the central region exhibits a somewhat more spherical shape than that of its E15A:2D counterpart. However, the magnitude of the angular velocities observed does not depend strongly on the initial choice of rotation law, since the equatorial regions of the precollapse core that undergo the greatest spin-up during collapse have almost identical Ω before collapse (eq. 1 and the discussion in §3). The bottom-left panel of Fig. 18 shows model E20A:2D's angular velocity snapshot at 200 ms after bounce. Model E20A has an initial core mass and density profile that are similar to those of the s20 progenitor (Fig. 2). Looking at Fig. 1, one notes that E20A's initial Ω profile exhibits an order-of-magnitude jump at around 1000 km, whereas E15A's angular velocity jumps at about 3 times that radius. This different behavior in the initial Ω profile and the initially longer central period of the E20A progenitor (Table 1) would naturally have led one to anticipate qualitative and quantitative differences in E20A:2D's angular velocity evolution when compared with that of models E15A:2D and s20A1000P2.34:2D. In fact, E20A:2D exhibits an appreciably different angular velocity profile. At lateral angles between about 25 and 155 degrees, the angular velocity is almost an order of magnitude lower than in the polar wedges. This can be understood as follows: At 200 ms after bounce, the high-angular velocity material that was inside a cylindrical radius of $\sim$1000 km has in the equatorial regions already accreted onto the PNS. What is then seen in the equatorial wedge is the angular velocity connected with material of initial cylindrical radii above $\sim$1000 km and, hence, of initially low angular velocity. However, in the polar region we see material of large initial spherical radius, but relatively small (below $\sim$1000 km) initial distance from the rotation axis. Hence, the higher angular velocity seen at 200 ms in the polar wedge.

In the bottom-right panel of Fig. 18 we display m15b6:2D's angular velocity distribution at 200 ms after bounce. This model's initial central iron core period is quite long (31.73 s)

and its iron core structure is similar to that of the older s11 and s15 progenitors (Woosley & Weaver 1995). Its iron core angular velocity profile exhibits the jumps at compositional boundaries which are characteristic of the set of rotating progenitors considered here. Again, arguing that the initial rotational profile is determining the PNS spin, we compare m15b6:2D with s11A1000P41.89:2D (bottom-right panel in Fig. 14). Even though model m15b6:2D has a shorter initial central period than s11A1000P41.89:2D, its central spheroidal bulge of high-angular velocity is smaller at 200 ms after bounce. A glance at Fig. 1 reveals the cause: m15b6's iron core is indeed spinning faster than s11A1000P41.89, though only in the inner $\sim$700 km of the precollapse iron core. At that radius, m15b6's Ω drops below the angular velocity in model s11A1000P41.89:2D due to the use of the rotation law of eq. (1) in the latter model.

Figures 19 and 20 show equatorial angular velocity and period profiles at 200 ms after bounce. Both figures contain a panel with Ω (P) on a logarithmic scale out to 300 km in equatorial radius and a more zoomed-in version showing only the inner 100 km. Ω (P) is drawn on a linear scale to more clearly display the differences between the individual models. We contrast the equatorial profiles of models s11A1000:2D, s15A1000:2D, and s20A1000:2D with P_0 set to 2.34 s with the Heger models E15A:2D, E20A:2D, and m15b6:2D. Above, we discussed the systematic changes of the PNS spin profile due to variations in the initial rotational configuration for a fixed progenitor structure. In the discussion of the two-dimensional angular velocity snapshots, we saw that progenitor mass and iron core structure appear to have only a secondary effect on the PNS's birth spin rate and rotational configuration. This is supported by the equatorial rotational profiles in Figs. 19 and 20. Models with similar initial (quantitative) rotational profile yield similar PNS rotational profiles, despite significant differences in their progenitor structures. Only in the linear-scale panels does one note differences that can be attributed to differences in the initial angular velocity distribution ("spherical" vs. "cylindrical" and rotation law vs. one-dimensional rotation). For example, we noted the interesting shape of E20A:2D's angular velocity distribution in Fig. 18. The early drop of Ω in the equatorial regions is reflected in the dropoff in equatorial angular velocity at about 30 km (clearly visible in the right panel of Fig. 19). Note that the initial discrete jumps of the angular velocity of models E15A:2D, E20A:2D, and m15b6:2D are naturally smoothed out during the two-dimensional collapse and postbounce evolution.

In Fig. 21, we compare the moment-of-inertia-weighted mean period $\bar{P}_{\rho 12}$ of models with different progenitor structures. For comparison, we enlarge the sample of models to include s11A1000P10.47:2D and E15A:2Ds. The evolution of $\bar{P}_{\rho 12}$ supports our assertion that progenitor structure has only a minor effect on the spin period of neutron stars at birth in our two-dimensional models. The magnitude of initial angular velocity in the part of the precollapse iron core that forms the homologous inner core during collapse is the most important parameter for the PNS spin. However, this assertion holds only for the early stages of the PNS evolution. It is possible that the rotational configuration could be influenced by, among other phenomena, late-time fall-back accretion whose rate and absolute accreted mass will depend on the progenitor mass density profile. Furthermore, black hole formation will become more probable with increasing progenitor mass, leading to a totally different scenario, possibly to a collapsar-type GRB (Woosley 1993; MacFadyen et al. 2001).

To conclude this section on our 2D axisymmetric models, we discuss the evolution of the rotation parameter β for different progenitor masses. In Fig. 22, we compare the postbounce β evolution for a representative set of models. β is an integral quantity, evaluated by integrals that encompass all grid points. Differences (and similarities) in the β evolution caused by progenitor structure and choice of initial angular velocity distribution and mapping are obvious. Models s11A1000P2.34:2D and s15A1000P2.34:2D are evolved with the same initial rotation law and start with identical P_0. Their iron core structure is very similar as well. Their β behavior turns out to be almost identical. Model s20A1000P2.34:2D is evolved using the same initial rotational configuration, but has a significantly more massive iron core with an initially lower central density. Its higher value of β at bounce and during its postbounce evolution is a consequence of the much greater angular momentum contained in s20A1000P2.34:2D's core and of its relatively high initial value of β. In Table 3, we list the total angular momentum contained in material above 10^{12} g cm^{-3} at the end of each model's numerical evolution. The high value of β at bounce is also in part a consequence of its initially lower core density. This results in a greater spin up of the inner core material during collapse. Model E20A:2D's initial central spin period is a bit shorter than s20A1000P2.34:2D's (2 s vs. 2.34 s), while its initial inner core density is slightly larger. E20A:2D's β is not much larger at bounce than s20A1000P2.34:2D's, but starts increasing with a greater rate postbounce. However, that increase is stopped about 10 ms after bounce when the initial profile's big jump in Ω at about 1000 km (Fig. 1) reaches small radii and the increase of rotational kinetic energy is abruptly slowed. Qualitatively, and to some extent quantitatively, this behavior can be inferred from the two-dimensional angular velocity snapshot presented in Fig. 18.

Overall, E15A:2D is the fastest model of our two-dimensional model set. Its initial central period is as low as 1.5 s and the *initial* value of β amounts to 0.5%. Its initial inner core density is considerably lower than for the slower or nonrotating 15 $M_\odot$ models (Fig. 2). It does, like E20A:2D, exhibit a discontinuity in Ω in its initial profile. However, this discontinuity is located at greater radii and does not advect in before the end of our simulation. All this explains the high β at bounce and the postbounce increase seen for this model. However, understanding what leads to the differences between models E15A:2D and E15A:2Ds requires a bit more involved discussion. In "shellular" rotation, the iron core angular velocity is set up to decrease roughly with r^{-2}, where r is the spherical radius (see eq. 1 and §3). In comparison with "cylindrical" rotation, off-equatorial grid points at a given distance ϖ from the rotation axis are set up with an initial angular velocity that is reduced by a factor of $\varpi/\sqrt{\varpi^2+z^2}$, where z is the cylindrical coordinate on the symmetry axis. Hence, there is less total angular momentum on E15A:2Ds' grid and its initial value of β is about 30% smaller than E15A:2D's. These facts determine this model's β evolution.

As expected, model E15A:2D reaches the greatest postbounce β of the entire set of two-dimensional models presented here. At the end of the calculation, β is 12.85% and is still increasing. During their late-postbounce evolution, models E15A:2D and s20A1000P2.34:2D and, perhaps, mod-

els E20A:2D and E15A:2Ds are likely to reach the classical threshold for secular rotational instability. However, it is unlikely that any of the models presented here will ever reach the threshold β at which classical high-T/|W| rotational instabilities would set in. Nevertheless, there are multiple models that may become unstable to the low-T/|W| instability of postbounce cores observed by Ott et al. (2005).

5. COMPARISON OF ONE- AND TWO-DIMENSIONAL SIMULATIONS

In §4.1 and §4.2, we presented the results of our one- and two-dimensional simulations separately. Here, we compare the two sets of simulations. Panel (a) of Fig. 23 shows the *equatorial* angular velocity profiles at 200 ms after bounce for models s11A1000P2.34, s11A1000P10.47, and E15A. Two-dimensional variant (:2D) profiles are the dashed lines, while one-dimensional variants (:1D) are the solid lines. For model E15A we also plot the version with "shellular" rotation (:2Ds). First, we note that the rotational profiles of E15A:2D and E15A:2Ds lie practically on top of each other. This is remarkable, but not entirely surprising if one recalls that the initial equatorial angular velocity profiles of these models are identical. However, Fig. 18 demonstrates that there are significant differences once one leaves the equator.

Comparing the :1D profiles to their :2D counterparts, we note that there is good agreement outside $\sim$50 km. With decreasing radius the :1D and :2D profiles for a given model begin to diverge. The two-dimensional models have less smooth profiles. The substructure in the equatorial profiles is created by angular momentum advection in convective plumes inside the protoneutron star and in the postshock region. Since convection is confined to small cylindrical radii in quickly spinning PNSs, the equatorial profiles of faster models overall are smoother and closer to those of their :1D counterparts than those of slow models that allow for more vigorous convection at greater cylindrical radii. Note that the jump in Ω visible in the :1D profile of E15A (green solid-line, at $\sim$20 km, also see Fig. 1) is smoothed out in its :2D counterpart.

In panel (b) of Fig. 23, we display the moment-of-inertia-weighted mean period $\bar{P}_{\rho 12}$ for the same set of models. $\bar{P}_{\rho 12}$ is an integral quantity based on a density criterion which takes into account the greater dimensionality of the :2D models. Model E15A is the fastest model for which we have :1D and :2D simulation data. Its initial central period is 1.5 s and it undergoes core bounce under strong centrifugal influence. The postbounce $\bar{P}_{\rho 12}$ evolutions of E15A:2D and E15A:2Ds differ significantly from those of their one-dimensional counterparts. At and after bounce, the two-dimensional PNSs are able to relax to greater PNS radii and energetically more favorable configurations than the spherically symmetric model. Hence, the :2D $\bar{P}_{\rho 12}$ of this (almost) rotationally supported model is larger than the :1D's. With increasing initial rotation period, rotational support for the PNS becomes less and less and the overall greater angular momentum in the :2D models leads to shorter PNS $\bar{P}_{\rho 12}$ s (see §3; "cylindrical" vs. "shellular" rotation; also see the discussion towards the end of §4.2).

The evolution of the rotation parameter β is shown in panel (c) of Fig. 23. Again, there are significant differences between :1D and :2D variants. For E15A, β is overestimated by the one-dimensional models and for the slower models s11A1000P2.34 and s11A1000P10.47 the one-dimensional models underestimate β. Model E15A:2Ds which is in "shellular" rotation reaches lower β than E15A:2D because there is less (total) angular momentum in the former. The explanation for the differences in β between one-dimensional and two-dimensional models is analogous to the explanation for the differences seen in the $\bar{P}_{\rho 12}$ evolution discussed above.

In panel (d) of Fig. 23, we display the mass-(spherical)radius relationship for selected :1D and :2D models. Here, the naive first assertion holds: the slower a model is, the more similar is its mass distribution to that of the corresponding :1D model and the better the :1D and :2D mass profiles agree. However, keep in mind that for fast :2D models that experience significant rotational flattening a mapping $M(r)$ will always be ambiguous.

We conclude that the overall characteristics and systematics of the mapping between initial model and rotational profile to the postbounce spin of the PNS are rendered with acceptable accuracy by the one-dimensional treatment of rotation. There can be, however, significant qualitative and quantitative differences between :2D and :1D in all models. In particular, we *do not* expect convergence of the :1D and :2D results with increasing P_0 since multi-dimensional effects, especially convection that becomes more vigorous in slower models, will always distinguish :2D evolution from :1D.

6. SIMPLE ESTIMATES OF THE FINAL NEUTRON STAR SPIN

The simulations presented in this paper cover only the very early stages of a neutron star's life. During tens to hundreds of seconds after bounce and a successful explosion, the neutron star will deleptonize and cool via neutrino emission. For the typical neutron star mass range of $\sim$1.2-1.6 $M_\odot$ (Fryer & Kalogera 2001; Thorsett & Chakrabarty 1999), Lattimer & Prakash (2001) find a radius of $\sim$12 km and a fiducial moment of inertia of $I = 0.35\ MR^2$ for a cold neutron star. Cold neutron stars are likely to be in solid-body rotation since this is the energetically most favorable configuration and viscous processes will most likely drive the neutron star into rigid rotation during its cooling phase.

A number of studies of stellar evolution (Heger et al. 2000, 2003b, 2005) and of rotating core-collapse and supernova evolution (Fryer & Heger 2000; Fryer & Warren 2004) have estimated the final neutron star spin period via

$$P_{NS} = 2\pi \frac{1}{(J/I)} \ . \qquad (5)$$

Here J is the supposed final total angular momentum and I is the moment of inertia obtained with the above prescription and a choice of neutron star mass and radius (typically M = 1.4 $M_\odot$ and R=12 km). For comparison with other studies, we estimate the asymptotic final neutron star spin of our models in the following manner. We consider our two-dimensional simulations and a representative subset of our one-dimensional simulations and choose M to be the mass of all material with a density above 10^{12} g cm^{-3} at 200 ms after bounce. We choose this time to ensure that we have one- and two-dimensional data for our estimates. Also that this is a sensible choice becomes apparent when looking at Fig. 12, which shows the mass interior to a given spherical radius at about 200 ms after bounce for representative models. $M_{\rho 12,200}$ encompasses the majority of the total mass on the grid, located interior to some tens of kilometers. We assume that a successful explosion removes the remaining matter and that

$M_{\rho 12,200}$ is the final neutron star mass. For simplicity, no further fall-back accretion or neutrino losses are considered. For the angular momentum in eq. (5), we choose $J_{\rho 12,200}$, which is the total angular momentum of mass $M_{\rho 12,200}$. We assume this angular momentum and mass to be conserved during the contraction to a final radius of 12 km. In addition, we compute the neutron star's rotation parameter β_{NS} = T/|W| and the ratio of the neutron star's angular velocity to the Keplerian break-up velocity, defined by $\Omega_K = \sqrt{GM/r^3}$. For β, we estimate the gravitational potential energy according to the prescription given in Lattimer & Prakash (2001):

$$|\mathrm{W}| \simeq Mc^2 \times 0.6\frac{GM}{Rc^2}/\left(1-0.5\frac{GM}{Rc^2}\right) . \qquad (6)$$

We summarize our estimates in Table 4. Neutron stars with $\beta > 50\%$ (Viral theorem limit) and angular velocity above the Keplerian break-up velocity cannot exist. For six of the two-dimensional models listed in Table 4 our estimate leads to a spin rate beyond break-up and to unphysically high values of β. Since the angular momentum contained in one-dimensional models is smaller than in the :2D models, only the two most extreme :1D models reach such high β and Ω/Ω_K. These models simply cannot form stable compact neutron stars, unless there are one or multiple mechanisms that remove angular momentum from the cooling neutron star. Otherwise, the neutron star will cool, but remain centrifugally hung-up with a disk of matter at Keplerian velocity. Two-dimensional models with initial central iron core spin period above $\sim$5 s may form stable neutron stars below the Keplerian limit (s11A1000P4.69:2D, s11A1000P10.47:2D, s11A∞P10.47:2D,s11A1000P41.89:2D,s11A1000P157.10:2D, and m15b6:2D). For the one-dimensional models, this initial period cut is somewhat lower, allowing iron cores with initial periods of down to $\sim$2 s to form stable neutron stars. However, keep in mind that the one-dimensional description of rotation is only approximate and underestimates the angular momentum in the PNS (see §5).

Only the overall slowest two-dimensional model (s11A1000P157.10:2D) produces a neutron star with a period in the ballpark of observed young pulsar periods (tens of milliseconds). Models s11A1000P41.89:2D and m15b6:2D yield neutron stars with $\sim$7 ms period. This number is in rough accord with the periods derived by Heger et al. (2003b) for progenitors with similar initial rotation period and angular momentum distribution. However, Heger et al. (2005) estimated a neutron star period of 11 ms for their m15b6 progenitor (cf. m15b6:1D's P_{NS} $\sim$ 14 ms). Fryer & Warren (2004) estimated for E15A and for a m15b6-like model neutron star periods of 0.91 ms and 17 ms, respectively. However, we note that in their three-dimensional simulations the PNS appears to continuously lose angular momentum after bounce. These authors do not provide a conclusive explanation for this phenomenon.

We have surveyed the parameter space of initial central iron core periods from $\sim$1.5 s to $\sim$160 s with one- and two-dimensional supernova simulations. Across the board, our estimates of the final neutron star spin periods, based on the two-dimensional simulations that handle rotation in a consistent manner, are shorter than found in previous studies. A large fraction of the two-dimensional models considered in this study produce cold, contracted neutron stars beyond the break-up spin rate. Given that observed young pulsar periods are between tens and hundreds of milliseconds, we conclude that there must be robust processes that efficiently spin down a neutron star before it emerges as a pulsar *or* that progenitor iron cores generically rotate more slowly than many of our progenitor models. We discuss in the following subsections a number of physical processes which could carry away or redistribute a significant amount of the angular momentum of the nascent neutron star.

6.1. *Viscous Processes*

In this paper, we have already considered a mechanism for spindown of PNSs: viscous angular momentum redistribution (by, e.g., the MRI)[8]. Because rotational energy scales with Ω^2, viscous heating scales with Ω^3, and the viscous timescale is proportional to Ω^{-1}, the multiple effects of viscosity are most noticeable in fast rotators (Thompson et al. 2005). However, even for our rapidly rotating models ($P_0 \lesssim 4$ s), our results (see §4.1 and Tables 2 and 4) indicate that viscous effects are not able to increase the spin period by more than a factor of 2 – 3 on 100 ms to 1 s timescales. Although potentially interesting, these processes are not sufficient to yield fully-contracted 10–20 ms neutron stars. For slower initial iron core spin periods ($P_0 \gtrsim 4$ s), viscous effects quickly become much less important.

6.2. *Secular and Dynamical Rotational Instabilities*

PNSs that spin with high enough β might undergo the low-T/|W| instability (for T/|W| $\gtrsim$ 8%, Ott et al. 2005) or the classical secular and dynamical rotational instabilities at higher T/|W|. These instabilities will put a lower limit on the neutron star spin of $\sim$1 ms (set by the value of β at which the star regains stability, which in turn depends on the degree of differential rotation and the equation of state), but cannot lead to a significant spindown of the neutron star.

6.3. *r-Modes/Gravitational Wave Emission*

Rossby-waves (r-modes) in rapidly rotating neutron stars are driven unstable by the emission of gravitational radiation. Consequently, stellar rotational energy is converted into both gravitational waves and r-mode energy (Andersson 1998; Lindblom et al. 2001). The spindown torque presented in Arras et al. (2003) is

$$\mathcal{M} \simeq (2\times 10^{49}\mathrm{dyn\,cm})\left(\frac{\alpha_e}{0.1}\right)\nu_{KHz}^{12} , \qquad (7)$$

where α_e is the saturation amplitude of the r-mode in dimensionless units and ν_{KHz} is the neutron star spin frequency (1/P) in units of kHz. With this, we estimate

$$\dot{\mathrm{P}} = \frac{1}{2\pi}\frac{\mathcal{M}}{I}\mathrm{P}^2 . \qquad (8)$$

Because of the low saturation level, α_e $\sim$0.1 (Arras et al. 2003), and the extreme spin-frequency dependence, r-modes can lead to a factor of two increase within a matter of days in the period of neutron stars that spin close to break-up, but will require millennia to slow down moderately rotating neutron stars (Arras et al. 2003; Heger et al. 2005).

[8] Other processes, such as the viscosity associated with convective turbulence, may also operate on the shear energy stored in differential rotation (Thompson et al. 2005)

6.4. *Neutrino Emission*

Neutrinos carry away ∼99% of the gravitational binding energy of a forming neutron star. Besides the possibility of a net linear momentum flux, which could be responsible for the observed neutron star birth kicks if sufficiently anisotropic, neutrinos also carry away angular momentum (Epstein 1978; Baumgarte & Shapiro 1998; Janka 2004). Assuming that the neutrinos are diffusing out of the neutrinosphere in all directions, Janka (2004) estimates that a maximum of ∼40% of the total angular momentum can be lost if the axis ratio of the PNS is close to one. Hence, this mechanism could — in the most optimistic case — lead to a factor-of-two spindown for a relatively slow PNS ($\bar{\mathrm{P}}_{\rho 12} \gtrsim 10$ ms).

6.5. *Rotation-Powered Supernovae*

The typical supernova explosion kinetic energy is near 10^{51} erg. The rotational energy stored in the PNSs in our models is easily calculated using $\mathrm{T} = 1/2\, J_{\rho,12}\, (2\pi/\bar{\mathrm{P}}_{\rho 12})$. Model s20A1000P2.34:2D has a rotational energy of $\sim 2 \times 10^{52}$ erg. If only 10% of this model's rotational energy is converted into radial kinetic energy, this could power the entire supernova explosion, as suggested in the "jet-driven" supernova mechanism (Akiyama et al. 2003; Akiyama & Wheeler 2005). In that picture, the PNS represents the fly-wheel that provides the rotational energy to drive (magneto-) hydrodynamic jets along the poles leading to a bipolar supernova explosion. If 10% of the rotational energy is dumped into the supernova, the PNS will spin down by not more than ∼5%. If, however, 50% of the rotational energy is imparted to the supernova, a spindown by ∼30% results.

6.6. *Magnetic Protoneutron Star Winds*

In the seconds after collapse and explosion, a thermal non-relativistic neutrino-driven wind emerges from the PNS (Duncan et al. 1986). If the PNS has a magnetar-strength ($\gtrsim 10^{14}$ – 10^{15} G; Duncan & Thompson 1992) large-scale surface magnetic field, then the wind material will be forced to corotate with the PNS. For rapid rotation, the wind is magneto-centrifugally whipped off of the stellar surface and the neutron star's angular momentum and rotational energy may be efficiently extracted (Thompson et al. 2004; Thompson 2003b). The spin period increases as $\dot{\mathrm{P}}/\mathrm{P} \approx 3(\dot{M}/M)(R_A/R_{NS})^2$, where $\dot{M}$ is the mass loss rate and R_A is the Alfvén radius, where the kinetic energy density of the wind first exceeds the magnetic energy density. If the wind carries away angular momentum at a constant rate over a time t, then the relative change in period is $\mathrm{P}/\mathrm{P}_{\mathrm{birth}} \sim \exp(\dot{\mathrm{P}}t/\mathrm{P})$. Assuming a 1.4 $\mathrm{M}_\odot$ PNS with a 2 ms period, a radius of 20 km, an Alfvén radius of 40 km, and a mass-loss rate of 10^{-3} $\mathrm{M}_\odot$ s^{-1} (Thompson et al. 2004), together with a 10 s wind duration, we obtain $\Delta\mathrm{P}/\mathrm{P}_{birth}$ of order 10%. Although this mechanism does not spin the PNS down significantly on a 10 s timescale, the non-relativistic wind carries of order 10^{51} erg in kinetic energy.

As any PNS cools and contracts, the neutrino luminosity decreases and the mass loss rate abates. As a consequence, for fixed magnetic field strength, the wind becomes Poynting-flux dominated and relativistic. For near-millisecond spin periods and magnetar-strength fields, this transition happens just seconds after the explosion commences (Thompson et al. 2004). Assuming a dipolar field configuration — probably pessimistic considering the fact that pulsar braking indices are observed to be less than 3 — the rotational energy loss rate is $\dot{E} \approx B^2 R^6 \Omega^4 / c^3$ so that the spindown timescale is just $\mathrm{P}/\dot{\mathrm{P}} \sim 1.7 \times 10^4$ s for a protoneutron star with R = 20 km, $B = 10^{14}$ G, P = 2 ms, and moment of inertia $I = 0.35 M R^2$. For these parameters, essentially all of the rotational energy can be lost to the relativistic wind in just tens of hours.

The two most obvious and fundamental problems with spinning down a millisecond PNS rapidly with non-relativistic or relativistic pulsar-like winds is that (1) normal neutron stars are not expected to be born with large-scale magnetar-strength fields and (2) if the PNS is efficiently spun down, the remnant should bear the signature of the $\sim 10^{52}$ ergs of rotational energy deposited within it. However, observations of generic young SNRs do not show evidence of such energy deposition.

6.7. *Fall-Back / Propeller Mechanism*

After a successful explosion there might be a phase during which the neutron star accretes a considerable amount of material that has failed to reach escape velocity in the shock-driven expulsion of the stellar envelope. MacFadyen et al. (2001) estimate the late-time (≥1000 s after explosion; Heger et al. 2005) fall-back accretion rate, based on the parameters of SN 1987A, to be

$$\dot{M} \equiv 2 \times 10^{26}\, t_5^{-5/3}\, \mathrm{g\ s^{-1}}\ , \tag{9}$$

where t_5 is the time in units of 10^5 s. If the then deleptonized, but possibly centrifugally-hung-up neutron star has a sufficiently strong magnetic field, its Alfvén radius can be greater then the radius at which the corotation angular velocity exceeds the Keplerian orbital speed. The infalling material is halted by magnetic forces at the Alfvén radius, spun up to corotation and, if $\Omega > \Omega_K$, expelled. The ejected matter carries away angular momentum and leads to a spindown of the neutron star. Heger et al. (2005), based on the work of Alpar (2001) (also see Romanova et al. 2004 for recent numerical results), estimate that this so-called propeller mechanism can very efficiently spin down neutron stars with surface magnetic field strengths above $\sim 2 \times 10^{13}$ G. Following Heger et al. (2005) we estimate the integrated deceleration as

$$\Delta\Omega \approx 30.6\, \mu_{30}^{4/5}\, \Omega_3^{3/5}\ , \tag{10}$$

where $\mu_{30} = B_{12} R_6^3$, B_{12} is the surface field in units of 10^{12} G, and R_6 is the neutron star radius in units of 10^6 cm. Ω_3 is the neutron star angular velocity in units of 10^3 rad s^{-1}. For a 2 ms period neutron star, hung-up with a 20 km radius and a conservative value of the surface magnetic field strength of 10^{12} G, the integrated change in Ω is ∼320 rad s^{-1}, corresponding to a change in the period of only 0.23 ms. With 15 times the magnetic field strength and all other parameters kept fixed, the integrated change in Ω would amount to ∼2800 rad s^{-1}, leaving behind a neutron star with a period of ∼18 ms. Given these numbers, there is great potential for the propeller mechanism to lead to a significant, order-of-magnitude spindown of the neutron star. However, it is not clear whether the propeller mechanism works in the way suggested in the literature. Furthermore, there is general ignorance concerning the magnetic field strength and topology in neutron stars. Also, there may not be much, or any, fallback for the majority of supernovae.

7. SUMMARY AND DISCUSSION

We have systematically investigated the mapping between presupernova (rotational) structure and the spin periods and rotational profiles of protoneutron stars. For this, we have performed a large set of rotating supernova core-collapse simulations in spherical- and axi-symmetry, using Newtonian gravity. For spherically-symmetric runs, we have employed the Boltzmann radiation-hydrodynamics code SESAME which has recently been upgraded to treat rotation in an approximate way. In addition, viscous dissipation and angular momentum redistribution have been included in a subset of our simulations. For models evolved in axisymmetry, we have made use of the multi-group flux-limited diffusion variant of the radiation-hydrodynamics code VULCAN/2D. For our simulations, we have taken 11, 15, and 20 $M_\odot$ (s11, s15, s20) presupernova models from the stellar evolution study of Woosley & Weaver (1995) and put them into rotation via a rotation law that assumes constant angular velocity either on cylindrical or spherical shells. In addition, we have performed simulations with the progenitor models E15A and E20A of Heger et al. (2000) and m15b6 of Heger et al. (2005). These progenitor models include a one-dimensional prescription for rotational evolution. We have considered initial central iron core spin periods between 1.25 s and 157.1 s and only central periods that map to angular velocities below the Keplerian break-up limit at all radii in each model at all times during the numerical evolution. The initial range of the rotation parameter β is set by a minimum of 7×10^{-5}% and a maximum of 0.88%.

In our one-dimensional simulations we find a roughly linear relationship between initial central iron core spin period and the protoneutron star spin. As an analysis tool we define a moment-of-inertia-weighted period ($\bar{P}_{\rho 12}$) for all material above 10^{12} g cm^{-3}. In Fig. 24, we plot $\bar{P}_{\rho 12}$ as a function of initial central spin period for a representative subset of our models. Each one-dimensional model (:1D) is marked with a solid box in the $P_0 - \bar{P}_{\rho 12}$ plane. The boxes of our s11A1000:1D model series are connected with solid lines to emphasize the $P_0 \rightarrow \bar{P}_{\rho 12}$ mapping. The graph is roughly fitted by a linear function with slope of 1.3 ms s^{-1}. Only in the fastest models (initial periods shorter than $\sim$2.5 s) do centrifugal effects lead to a noticable deviation from the displayed simple linear relationship. In considering the discrete profiles, we identify a region of near-solid body rotation inside the nuclear-density region of the PNS out to a radius of $\sim$10 km or $\sim$0.5 $M_\odot$ in mass coordinate. This is a consequence of quasi-homologous collapse. Outside this region PNSs are strongly differentially rotating. In a typical fast model, the angular velocity drops from $\sim$2500 rad s^{-1} at 20 km to a few rad s^{-1} at 100 km. The energy stored in differential rotation can efficiently be tapped by viscous processes. We have considered the MRI as one such process and have included its action in a subset of our one-dimensional models (the ":1Dv" models; see §2.1). As displayed in Fig. 8, viscosity leads to a spin down of the central part of the PNS and enforces rigid rotation out to 50 kms and beyond. The viscous timescale is proportional to Ω^{-1} and the viscous heating rate scales with Ω^3. Hence, the efficiency of viscosity in reducing the rotational shear, in moving angular momentum out, and in spinning down the PNS is only great for rapidly rotating models. In Fig. 24, open rhombi symbolize the models that include viscous angular momentum redistribution. Those rhombi corresponding to models of the s11A1000:1D series are connected with dashed lines. Comparing the two graphs in Fig. 24, we note that the inclusion of viscosity leads to slower $\bar{P}_{\rho 12}$ for all models. The relative spin down is greatest for models below $\sim$3 ms period, but no model is slowed by more than a factor of two in $\bar{P}_{\rho 12}$. Models with long initial periods are slowed by only a few to ten percent.

Our two-dimensional, axisymmetric simulations allow for a more consistent and more correct treatment of rotational effects during core collapse and the postbounce phase. The results indicate that the one-dimensional approach taken by us and other groups is neither very good nor very bad for any of the precollapse rotation rates considered here. In fast two-dimensional models convective motions are confined to small cylindrical radii. Hence equatorial profiles of fast :2D models exhibit less substructure and are closer to their :1D counterparts than slower models in which convection is more vigorous out to larger radii. For slow to moderate initial spin rate, the two-dimensional simulation results also yield a mapping of $P_0 \rightarrow \bar{P}_{\rho 12}$ which is roughly linear for large P_0 and that deviates from linearity at lower values of P_0; the correct treatment of centrifugal effects results in less compact and more oblate PNSs.

In comparing our 2D radiation-hydrodynamics, MGFLD models with purely hydrodynamic results, we find that the large-scale, coherent, and repeated expansion-collapse-bounce cycles observed in purely hydrodynamic calculations are critically damped in simulations that include neutrino radiative transfer and microphysics. This is an important finding because of its implication for the gravitational wave signature of rotating stellar core collapse and bounce. Contrary to current belief (Zwerger & Müller 1997; Dimmelmeier et al. 2002; Kotake et al. 2003; Ott et al. 2004), the collapse and bounce of even fast rotators (like E15A with P_0=1.5 s and an initial β of 0.42%) will not yield gravitational waves of large amplitude and energy emission. As with slowly rotating models, the greatest part of the gravitational wave emission will come from postbounce large-scale convective motions in the postshock region and in the PNS and, possibly, from anisotropic neutrino emission (Burrows & Hayes 1996; Ott et al. 2004; Müller et al. 2004).

At the end of our two-dimensional simulations (on average 240 ms after core bounce), we find mean PNS periods in the range from 4.7 ms to 140 ms. The final $\bar{P}_{\rho 12}$ depends mainly on the inner precollapse iron core spin period. Differences in progenitor mass, structure, and rotation law lead to only first-order corrections in $\bar{P}_{\rho 12}$. However, differences in progenitor mass and structure have a strong impact on other observables; the more massive a progenitor, the greater are its final PNS mass, angular momentum, and rotation parameter β. The maximum values of β range between 5×10^{-2}% and 12.9% in our two-dimensional simulations. At postbounce times, β increases roughly linearly as the PNS simultaneously accretes more material and becomes more compact. During its cooling and deleptonization phase, a PNS with a birth period below $\sim$5 ms will surpass the β-threshold values for classical secular and dynamical rotational instability ($\sim$14% and $\sim$27%, respectively). It is, however, possible that they experience a low-T/|W| instability even earlier (Ott et al. 2005).

To compare with previous, though more approximate, studies, we have taken the PNS configurations of our simulations at 200 ms after core bounce and extrapolated the spin periods

and βs to final, deleptonized, and cold states. For the same (or very similar) initial conditions, our models yield shorter neutron star periods than previous studies (Heger et al. 2000; Fryer & Heger 2000; Heger et al. 2003b, 2005). Any model with initial iron core period below $\sim$10 s leads to a neutron star with a submillisecond period, spinning with surface velocities close to break-up. Since young pulsars enter the $P - \dot{P}$ diagram at periods of many tens to hundreds of milliseconds (Kaspi & Helfand 2002), we have surveyed a number of possible spindown mechanisms that could transform a young millisecond-period neutron star into one with a period in agreement with observations. These include viscous angular momentum redistribution by the MRI or another viscous process, rotational hydrodynamic instabilities, r-modes, neutrino angular momentum transport, rotation-powered explosions, early magnetic-dipole (pulsar) emission, neutrino-driven magnetic winds, and the propeller mechanism. We find that none of the processes considered is robust enough to spin down a millisecond PNS to a tens-of-milliseconds pulsar. The most promising is the propeller mechanism that removes angular momentum from the neutron star by expelling fall-back material at the Alfvén radius, while not requiring magnetic field strengths in excess of several 10^{12} G to a few 10^{13} G. However, there remain many open questions concerning the physical details involved and whether fallback is even generic has not been resolved.

Hence, we conclude that, if a pulsar were born rapidly rotating, nonaxisymmetric rotational hydrodynamic instabilities and other proprosed mechanisms of spindown may not be adequate to cause the requisite spindown from rapid to observed rates. In addition, it is clear that spindown mechanisms that employ magnetic fields would also transfer a rapidly rotating PNS's kinetic energy to the envelope debris, in contrast with the observational estimates of generic supernova and supernova remnant energies (§6.6). Therefore, on the basis of our theoretical calculations of the mapping between initial and final spins, likely spindown mechanisms, and the observational constraints from pulsars and supernova energetics, we conclude that the progenitor spin rates of the cores of the massive stars that give birth to observed neutron stars and pulsars are low, with corresponding periods on average greater than $\sim$50 seconds. The associated average neutron star would thereby be born with a period no less than $\sim$10 ms and with $\beta \lesssim 2\%$. However, the final neutron star spin is a function of the progenitor mass. Some very massive progenitors might lead to very fast and massive neutron stars that might evolve to collapsars and rotation-powered GRBs.

Figure 25 shows equatorial specific angular momentum profiles at 200 ms after core bounce for a representative subset of our models evolved in axisymmetry with VULCAN/2D. Note that models of similar initial central iron core P_0 yield very similar specific angular velocity profiles, despite differences in progenitor structure. Model s11A∞P10.47:2D, which is initially set up in solid-body rotation, yields outside some tens of kilometers specific angular momenta as high as found in differentially rotating models with up to 5 times shorter initial central periods. Given the estimates of Heger & Woosley (2003), the specific angular momenta of our models with initial central periods below $\sim$10 s are sufficient to rotationally support an accretion disk around a Kerr black hole.

Finally, we point out that even though this study has advanced our knowledge concerning the birth spin periods and rotational profiles of neutron stars, and their dependence on initial iron core spin and structure, many important questions remain unanswered. We have followed the PNSs for only a few hundred milliseconds after formation. We have not tracked the supernova explosion through the stellar envelope and subsequent fall-back accretion. We have not included general relativistic effects, nor magneto-hydrodynamics. Fully consistent, three-dimensional, radiation-magneto-hydrodynamics simulations in general relativity will be required to reveal in detail the evolution from a very young PNS to the final rotating pulsar (or black hole).

We acknowledge discussions with and help from Jeremiah Murphy, Itamar Lichtenstadt, Casey Meakin, and Ed Seidel. Importantly, we acknowledge support for this work from the Scientific Discovery through Advanced Computing (SciDAC) program of the DOE, grant number DE-FC02-01ER41184, and from the NSF, grant number AST-0504947. E. L. acknowledges support from the Israel Science Foundation under grant 805/04. R.W. thanks the Institute of Astronomy of the ETH Zurich for providing part-time office space and C.D.O. thanks the Albert-Einstein-Institut for financial support and for providing CPU time on their Peyote Linux cluster. T.A.T. acknowledges support by NASA through Hubble Fellowship grant #HST-HF-01157.01-A, awarded by the Space Telescope Science Institute, which is operated by the Association of Universities for Research in Astronomy, Inc., for NASA, under contract NAS 5-26555. Finally, we thank Jeff Fookson and Neal Lauver of the Steward Computer Support Group for their invaluable help with the local Beowulf clusters and acknowledge the use of the NERSC/LBNL/seaborg and ORNL/CCS/RAM machines. Movies and additional still frames associated with this work can be obtained upon request from the authors.

REFERENCES

Akiyama, S., Wheeler, J. C., Meier, D. L., & Lichtenstadt, I. 2003, ApJ, 584, 954
Akiyama, S., & Wheeler, J. C. 2005, ApJ, 629, 414
Alpar, M. A. 2001, ApJ, 554, 1245
Andersson, N. 1998, ApJ, 502, 708
Arras, P., Flanagan, E. E., Morsink, S. M., Schenk, A. K., Teukolsky, S. A., & Wasserman, I. 2003, ApJ, 591, 1129
Balbus, S. A., & Hawley, J. F. 1991, ApJ, 376, 214
Balbus, S. A., & Hawley, J. F. 1994, MNRAS, 266, 769
Baumgarte, T. W., & Shapiro, S. L. 1998, ApJ, 504, 431
Bethe, H. A., & Wilson, J. R. 1985, ApJ, 295, 14
Bruenn, S. W. 1985, ApJS, 58, 771
Buras, R., Rampp, M., Janka, H.-T., & Kifonidis, K. 2003, Phys. Rev. Lett., 90, 241101
Burrows, A., & Hayes, J. 1996, Phys. Rev. Lett., 76, 352
Burrows, A., Hayes, J., & Fryxell, B. A. 1995, ApJ, 450, 830
Burrows, A., & Lattimer, J. M. 1986, ApJ, 307, 178
Burrows, A., Young, T., Pinto, P., Eastman, R., & Thompson, T. A. 2000, ApJ, 539, 865
Centrella, J., New, K., Lowe, L., & Brown, J. 2001, ApJ, L550
Dimmelmeier, H., Font, J., & Müller, E. 2002, A&A, 393, 523
Duncan, R. C., Shapiro, S. L., & Wasserman, I. 1986, ApJ, 309, 141
Duncan, R. C., & Thompson, C. 1992, ApJ, 392, L9
Epstein, R. 1978, ApJ, 223, 1037

Fryer, C. L. 2004, ApJ, 601, L175
Fryer, C. L. 1999, ApJ, 522, 413
Fryer, C. L., & Heger, A. 2000, ApJ, 541, 1033
Fryer, C. L., & Kalogera, V. 2001, ApJ, 554, 548
Fryer, C. L., & Warren, M. S. 2004, ApJ, 601, 391
Fukuda, I. 1982, PASP, 94, 271
Heger, A., Langer, N., & Woosley, S. E. 2000, ApJ, 528, 368
Heger, A., & Woosley, S. E. 2003, AIP Conf. Proc. 662: Gamma-Ray Burst and Afterglow Astronomy 2001: A Workshop Celebrating the First Year of the HETE Mission, 662, 214
Heger, A., Fryer, C. L., Woosley, S. E., Langer, N., & Hartmann, D. H. 2003a, ApJ, 591, 288
Heger, A., Woosley, S. E., Langer, N., & Spruit, H. C. 2003b, Stellar Rotation. Proceedings IAU Symposium No. 215
Heger, A., Woosley, S. E., & Spruit, H. C. 2005, ApJ, 626, 350
Herant, M., Benz, W., Hix, W. R., Fryer, C. L., & Colgate, S. A. 1994, ApJ, 435, 339
Ho, W. C. G., & Lai, D. 2000, ApJ, 543, 386
Janka, H.-T., Buras, R., & Rampp, M. 2003, Nuc. Phys. A, 718, 269
Janka, H.-T. 2004, in "Young Neutron Stars and Their Environments", Proceedings, IAU Symposium 218
Janka, H.-T., Scheck, L., Kifonidis, K., Müller, E., & Plewa, T. 2005, in: The Fate of the Most Massive Stars, Proc. Eta Carinae Science Symposium (Jackson Hole, May 2004)
Kaspi, V. M., & Helfand, D. J. 2002, Neutron Stars in Supernova Remnants, ASP Conference Series, Vol. 271, edited by P. O. Slane & B. M. Gaensler
Keil, W., & Janka, H.-T. 1995, A&A, 296, 145
Kotake, K., Yamada, S., & Sato, K. 2003, Phys. Rev. D, 68, 044023
Lai, D., Chernoff, D. F., & Cordes, J. M. 2001, ApJ, 549, 1111
Lattimer, J. M., & Prakash, M. 2001, ApJ, 550, 426
Lattimer, J. M., & Swesty, F. D. 1991, Nucl. Phys. A, 535, 331
Liebendörfer, M., Mezzacappa, A., & Thielemann, F. 2001, Phys. Rev. D, 63, 104003
Lindblom, L., Tohline, J. E., & Vallisneri, M. 2001, Phys. Rev. Lett., 86, 1152
Livne, E. 1993, ApJ, 412, 634
Livne, E., Burrows, A., Walder, R., Lichtenstadt, I., & Thompson, T. A. 2004, ApJ, 609, 277
Lyne, A. G., & Graham-Smith, F. 1998, Pulsar astronomy, Cambridge, U.K.: Cambridge University Press.
Lyne, A. G., & Lorimer, D. R. 1994, Nature, 369, 127
MacFadyen, A. I., Woosley, S. E., & Heger, A. 2001, ApJ, 550, 410
Müller, E., Rampp, M., Buras, R., Janka, H.-T., & Shoemaker, D. H. 2004, ApJ, 603, 221
Marshall, F. E., Gotthelf, E. V., Zhang, W., Middleditch, J., & Wang, Q. D. 1998, ApJ, 499, L179
Martinez-Pinedo, G., Liebendoerfer, M., & Frekers, D. 2004, astro-ph/0412091
Mezzacappa, A., Liebendörfer, M., Messer, O. E., Hix, W. R., Thielemann, F., & Bruenn, S. W. 2001, Phys. Rev. Lett., 86, 1935
Mönchmeyer, R., Schäfer, G., Müller, E., & Kates, R. 1991, A&A, 246, 417
Nomoto, K., Tominaga, N., Umeda, H., Maeda, K., Ohkubo, T., Deng, J., & Mazzali, P. A. 2005, ASP Conf. Ser. 332: The Fate of the Most Massive Stars, 332, 384
Ostriker, J. P., & Gunn, J. E. 1969, ApJ, 157, 1395
Ott, C. D., Burrows, A., Livne, E., & Walder, R. 2004, ApJ, 600, 834
Ott, C. D., Ou, S., Tohline, J. E., & Burrows, A. 2005, ApJ, 625, L119
Pons, J. A., Reddy, S., Prakash, M., Lattimer, J. M., & Miralles, J. A. 1999, ApJ, 513, 780
Rampp, M., & Janka, H.-T. 2002, A&A, 396, 361
Romanova, M. M., Ustyugova, G. V., Koldoba, A. V., & Lovelace, R. V. E. 2004, ApJ, 616, L151
Saijo, M., Baumgarte, T. W., & Shapiro, S. L. 2003, ApJ, 595, 352
Scheck, L., Plewa, T., Janka, H.-T., Kifonidis, K., & Müller, E. 2004, Phys. Rev. Lett., 92, 011103
Shibata, M., Karino, S., & Eriguchi, Y. 2002, MNRAS, 334, L27
—. 2003, MNRAS, 343, 619
Spruit, H. C., & Phinney, E. S. 1998, Nature, 393, 139
Tassoul, J.-L. 1978, Theory of Rotating Stars (Princeton U. S. A.: Princeton University Press)
Thompson, T. A. 2003a, ApJ, 585, L33
—. 2003b, ApJ, 585, L33
Thompson, T. A., Burrows, A., & Pinto, P. A. 2003, ApJ, 592, 434
Thompson, T. A., Chang, P., & Quataert, E. 2004, ApJ, 611, 380
Thompson, T. A., Quataert, E., & Burrows, A. 2005, ApJ, 620, 861
Thorsett, S. E., & Chakrabarty, D. 1999, ApJ, 512, 288
Walder, R., Burrows, A., Ott, C. D., Livne, E., Lichtenstadt, I., & Jarrah, M. 2005, ApJ, 626, 317
Watts, A. L., & Andersson, N. 2002, MNRAS, 333, 943
Woosley, S. E. 1993, ApJ, 405, 273
Woosley, S. E., & Weaver, T. A. 1995, ApJS, 101, 181
Zwerger, T., & Müller, E. 1997, A&A, 320, 209

TABLE 1
INITIAL MODELS

Progenitor	ZAMS Mass ($M_\odot$)	R_{Fe} (10^8 cm)	M_{Fe} ($M_\odot$)	Model Name	Evolution Type	A (km)	Ω_0 (rad s^{-1})	P_0 (s)
s11	11	1.35	1.32					
				s11A1000P1.25:1D[a]	SESAME	1000	5.03	1.25
				s11A1000P2.00:1D[a]	SESAME	1000	3.14	2.00
				s11A1000P2.34:1D	SESAME	1000	2.68	2.34
				s11A1000P3.00:1D[a]	SESAME	1000	2.09	3.00
				s11A1000P4.00:1D[a]	SESAME	1000	1.57	4.00
				s11A1000P5.00:1D[a]	SESAME	1000	1.26	5.00
				s11A1000P8.00:1D[a]	SESAME	1000	0.79	8.00
				s11A1000P10.47:1D	SESAME	1000	0.60	10.47
				s11A1000P2.00:1Dv[a]	SESAME V	1000	3.14	2.00
				s11A1000P2.34:1Dv	SESAME V	1000	2.68	2.34
				s11A1000P3.00:1Dv[a]	SESAME V	1000	2.09	3.00
				s11A1000P4.00:1Dv[a]	SESAME V	1000	1.57	4.00
				s11A1000P10.47:1Dv	SESAME V	1000	0.60	10.47
				s11A∞P10.47:1D	SESAME	∞	0.60	10.47
				s11A∞P10.47:1Dv	SESAME V	∞	0.60	10.47
				s11A1000P2.34:2D[b]	VULCAN	1000	2.68	2.34
				s11A1000P2.34:2Dh	VULCAN H	1000	2.68	2.34
				s11A1000P4.69:2D[b]	VULCAN	1000	1.34	4.69
				s11A1000P10.47:2D[b]	VULCAN	1000	0.60	10.47
				s11A1000P10.47:2Dh	VULCAN H	1000	0.60	10.47
				s11A1000P41.89:2D[b]	VULCAN	1000	0.15	41.89
				s11A1000P157.10:2D[b]	VULCAN	1000	0.04	157.10
				s11A∞P10.47:2D	VULCAN	∞	0.60	10.47
s15	15	1.16	1.28					
				s15A1000P2.34:1D	SESAME	1000	2.68	2.34
				s15A1000P10.47:1D	SESAME	1000	0.60	10.47
				s15A1000P2.34:1Dv	SESAME V	1000	2.68	2.34
				s15A1000P10.47:1Dv	SESAME V	1000	0.60	10.47
				s15A1000P2.34:2D	VULCAN	1000	2.68	2.34
s20	20	2.21	1.92					
				s20A1000P2.34:1D	SESAME	1000	2.68	2.34
				s20A1000P10.47:1D	SESAME	1000	0.60	10.47
				s20A1000P2.34:1Dv	SESAME V	1000	2.68	2.34
				s20A1000P10.47:1Dv	SESAME V	1000	0.60	10.47
				s20A1000P2.34:2D	VULCAN	1000	2.68	2.34
E15A	15	2.22	1.62					
				E15A:1D[a]	SESAME	-	4.18	1.50
				E15A:1Dv[a]	SESAME V	-	4.18	1.50
				E15A:2D	VULCAN	-	4.18	1.50
				E15A:2Ds	VULCAN S	-	4.18	1.50
E20A	20	2.78	1.84					
				E20A:1D	SESAME	-	3.13	2.00
				E20A:1Dv	SESAME V	-	3.13	2.00
				E20A:2D	VULCAN	-	3.13	2.00
m15b6	15	1.95	1.47					
				m15b6:1D	SESAME	-	0.198	31.73
				m15b6:1Dv	SESAME V	-	0.198	31.73
				m15b6:2D	VULCAN	-	0.198	31.73

NOTE. — List of models included in this study. The supernova progenitor star models s11, s15 and s20 are taken from Woosley & Weaver (1995); E15A and E20A are from Heger et al. (2000) and m15b6 is from Heger et al. (2005). Models E15A, E20A, and m15b6 include rotation using a one-dimensional prescription for angular momentum evolution. Centrifugal force terms were included up to the end of core carbon burning. s11, s15, and s20 are non-rotating and are forced to rotate by the rotation law given in eq. (1). R_{Fe} is the radius of the iron core (determined by the discontinuity in Y_e at the outer edge of the iron core). M_{Fe} is the mass of the iron core. Evolution type denotes the way a model is evolved. SESAME stands for spherically symmetric evolution with the SESAME code, SESAME V indicates that dissipative angular momentum redistribution is switched on, VULCAN means two-dimensional simulation with MGFLD, VULCAN S stands for two-dimensional simulation with MGFLD, but *shellular* rotation (§2.2), and VULCAN H means purely hydrodynamic two-dimensional simulation without neutrinos. A is the parameter governing the degree of differential rotation (eq. 1). Ω_0 and P_0 are the initial central angular velocity and spin period, respectively. All progenitor models already have an initial infall velocity profile when they are mapped onto our computational grid. Nothing artificial is done to initiate collapse.

[a]Previously published/discussed in Thompson et al. (2005)

[b]Previously published/discussed in Walder et al. (2005)

TABLE 2
SUMMARY OF RESULTS: ONE-DIMENSIONAL MODELS

Model Name	t_f - t_b (ms)	P_0 (s)	$\bar{P}_{\rho 12,f}$ (ms)	$M_{\rho 12,f}$ ($M_\odot$)	$J_{\rho 12,f}$ (10^{49} erg s)	β_i (%)	β_f (%)
s11A1000P1.25:1D	587	1.25	3.11	1.07	1.172	$8.80\cdot10^{-1}$	18.44
s11A1000P2.00:1D	629	2.00	3.50	1.28	1.127	$3.44\cdot10^{-1}$	10.45
s11A1000P2.34:1D	630	2.34	3.85	1.32	1.091	$2.51\cdot10^{-1}$	7.96
s11A1000P3.00:1D	588	3.00	4.72	1.35	0.901	$1.53\cdot10^{-1}$	5.10
s11A1000P4.00:1D	541	4.00	5.94	1.37	0.706	$8.60\cdot10^{-2}$	2.98
s11A1000P5.00:1D	608	5.00	6.94	1.39	0.586	$5.50\cdot10^{-2}$	1.97
s11A1000P8.00:1D	532	8.00	11.16	1.39	0.366	$2.15\cdot10^{-2}$	0.759
s11A1000P10.47:1D	549	10.47	14.28	1.39	0.283	$1.25\cdot10^{-2}$	0.448
s11A1000P2.00:1Dv	500	2.00	6.72	1.13	0.392	$3.44\cdot10^{-1}$	2.25
s11A1000P2.34:1Dv	437	2.34	7.18	1.16	0.428	$2.51\cdot10^{-1}$	2.42
s11A1000P3.00:1Dv	1037	3.00	6.13	1.29	0.500	$1.53\cdot10^{-1}$	1.97
s11A1000P4.00:1Dv	573	4.00	7.42	1.33	0.524	$8.60\cdot10^{-2}$	1.99
s11A1000P10.47:1Dv	549	10.47	14.93	1.39	0.271	$1.25\cdot10^{-2}$	0.416
s11A∞P10.47:1D	571	10.47	9.18	1.34	0.428	$5.51\cdot10^{-2}$	1.59
s11A∞P10.47:1Dv	570	10.47	9.41	1.34	0.415	$5.51\cdot10^{-2}$	1.17
s15A1000P2.34:1D	612	2.34	3.95	1.39	1.197	$2.45\cdot10^{-1}$	7.92
s15A1000P10.47:1D	562	10.47	13.70	1.47	0.316	$1.22\cdot10^{-2}$	0.468
s15A1000P2.34:1Dv	612	2.34	6.76	1.24	0.501	$2.45\cdot10^{-1}$	2.51
s15A1000P10.47:1Dv	563	10.47	14.13	1.46	0.307	$1.22\cdot10^{-2}$	0.447
s20A1000P2.34:1D	462	2.34	3.48	1.84	2.820	$3.53\cdot10^{-1}$	15.26
s20A1000P10.47:1D	349	10.47	11.30	1.85	0.645	$1.76\cdot10^{-2}$	0.875
s20A1000P2.34:1Dv	365	2.34	6.80	1.40	0.749	$3.53\cdot10^{-1}$	4.32
s20A1000P10.47:1Dv	347	10.47	11.86	1.85	0.620	$1.76\cdot10^{-2}$	0.740
E15A:1D	780	1.50	2.91	1.53	2.064	$4.95\cdot10^{-1}$	17.45
E15A:1Dv	639	1.50	5.76	1.25	0.513	$4.95\cdot10^{-1}$	2.50
E20A:1D	461	2.00	3.43	1.84	2.213	$2.85\cdot10^{-1}$	12.52
E20A:1Dv	361	2.00	6.92	1.46	0.805	$2.85\cdot10^{-1}$	3.95
m15b6:1D	589	31.73	57.98	1.50	0.077	$7.77\cdot10^{-4}$	0.0280
m15b6:1Dv	589	31.73	58.21	1.50	0.076	$7.77\cdot10^{-4}$	0.0234

NOTE. — Numerical results for the supernova simulations performed with SESAME in spherical symmetry. Model initial conditions are detailed in Table 1. Here, t_f - t_b denotes the time elapsed after core bounce to when we stop the calculation. P_0 is the initial central rotation period and $\bar{P}_{\rho 12,f}$ is the mean PNS rotation period (for material with $\rho \geq 10^{12}$ g cm^{-3} (defined by eq. 3) at the end of the simulation. $M_{\rho 12,f}$ is the integrated mass of all material above the same density threshold at the end of the numerical calculation and $J_{\rho 12,f}$ is the angular momentum associated with $M_{\rho 12,f}$. β_i and β_f represent the values of T/|W| at the initial stage and at the end of the simulation, respectively.

TABLE 3
SUMMARY OF RESULTS: TWO-DIMENSIONAL MODELS

Model Name	t_f - t_b (ms)	P_0 (s)	$\bar{P}_{\rho 12,f}$ (ms)	$M_{\rho 12,f}$ ($M_\odot$)	$J_{\rho 12,f}$ (10^{49} erg s)	β_i (%)	β_f (%)
s11A1000P2.34:2D	197	2.34	4.74	1.17	1.522	$3.14\cdot10^{-1}$	6.72
s11A1000P2.34:2Dh	150	2.34	4.86	1.16	1.436	$3.14\cdot10^{-1}$	6.12
s11A1000P4.69:2D	262	4.69	5.63	1.28	0.998	$8.35\cdot10^{-2}$	2.64
s11A1000P10.47:2D	293	10.47	10.05	1.33	0.489	$1.53\cdot10^{-2}$	0.694
s11A1000P10.47:2Dh	294	10.47	10.44	1.13	0.301	$1.53\cdot10^{-2}$	0.498
s11A1000P41.89:2D	319	41.89	37.79	1.33	0.123	$1.04\cdot10^{-3}$	0.0536
s11A1000P157.10:2D	318	157.10	139.63	1.33	0.033	$7.00\cdot10^{-5}$	0.00451
s11A∞P10.47:2D	192	10.47	9.50	1.26	0.613	$5.35\cdot10^{-2}$	1.26
s15A1000P2.34:2D	215	2.34	4.69	1.18	1.563	$3.07\cdot10^{-1}$	7.00
s20A1000P2.34:2D	238	2.34	4.98	1.42	3.351	$5.08\cdot10^{-1}$	12.67
E15A:2D	217	1.50	5.12	1.28	2.801	$6.45\cdot10^{-1}$	12.85
E15A:2Ds	243	1.50	4.73	1.37	2.738	$4.64\cdot10^{-1}$	10.75
E20A:2D	211	2.00	5.40	1.49	3.185	$4.17\cdot10^{-1}$	10.76
m15b6:2D	195	31.73	50.25	1.39	0.129	$1.03\cdot10^{-3}$	0.0533

NOTE. — Same as Table 2, but listing results of our simulations performed with VULCAN/2D in axisymmetry.

TABLE 4
FINAL NEUTRON STAR SPIN ESTIMATES

Model Name	P_0 (s)	$M_{\rho 12,200}$ ($M_\odot$)	$J_{\rho 12,200}$ (10^{49} erg s)	P_{NS} (ms)	β_{NS} (%)	Ω_{NS}/Ω_K
s11A1000P2.34:2D	2.34	1.17	1.522	0.48	50.65	1.37
s11A1000P4.69:2D	4.69	1.25	0.992	0.85	15.16	0.75
s11A1000P10.47:2D	10.47	1.28	0.443	1.82	3.25	0.35
s11A1000P41.89:2D	41.89	1.29	0.113	7.19	0.21	0.09
s11A1000P157.10:2D	157.10	1.29	0.030	27.10	0.02	0.02
s11A∞P10.47:2D	10.47	1.26	0.613	1.30	6.54	0.49
s15A1000P2.34:2D	2.34	1.18	1.550	0.48	51.25	1.38
s20A1000P2.34:2D	2.34	1.27	3.098	0.28	129.01	2.20
E15A:2D	1.50	1.27	2.724	0.29	126.05	2.17
E15A:2Ds	1.50	1.33	2.553	0.33	96.01	1.89
E20A:2D	2.00	1.47	3.104	0.30	104.13	1.98
m15b6:2D	31.73	1.39	0.129	6.79	0.21	0.09
s11A1000P2.34:1D	2.34	1.15	0.762	0.95	13.39	0.70
s11A1000P2.34:1Dv	2.34	1.06	0.378	1.77	4.23	0.39
s11A1000P10.47:1D	10.47	1.26	0.211	3.76	0.77	0.17
s11A1000P10.47:1Dv	10.47	1.25	0.200	3.94	0.71	0.16
s11A∞P10.47:1D	10.47	1.23	0.295	2.63	1.63	0.25
s11A∞P10.47:1Dv	10.47	1.22	0.275	2.80	1.45	0.23
s15A1000P2.34:1D	2.34	1.19	0.790	0.95	12.96	0.69
s15A1000P2.34:1Dv	2.34	1.09	0.416	1.65	4.71	0.42
s20A1000P2.34:1D	2.34	1.41	1.622	0.55	32.35	1.10
s20A1000P2.34:1Dv	2.34	1.15	0.527	1.38	6.41	0.49
E15A:1D	1.5	1.21	1.271	0.60	31.86	1.09
E15A:1Dv	1.5	1.01	0.378	1.68	4.91	0.42
E20A:1D	2.00	1.49	1.465	0.64	22.24	0.92
E20A:1Dv	2.00	1.19	0.560	1.34	6.51	0.49
m15b6:1D	31.37	1.33	0.059	14.21	0.05	0.04
m15b6:1Dv	31.37	1.33	0.058	14.45	0.05	0.04

NOTE. — Overview table listing the key quantities for the cold neutron star spin estimates of §6. P_0 is the initial central rotation period, $M_{\rho 12,200}$ is the mass of all material with density $\rho \geq 10^{12}$ g cm^{-3} at 200 ms after bounce, and $J_{\rho 12,200}$ is the total angular momentum contained in that material. P_{NS} is the final neutron star spin estimate according to eq. (5). β_{NS} is an estimate of the neutron star rotation parameter and Ω_{NS}/Ω_K is the ratio of the neutron star's angular velocity to the Keplerian break-up velocity defined by $\sqrt{GM/r^3}$. Neutron stars with $\Omega_{NS}/\Omega_K \gtrsim 1.0$ or $\beta \gtrsim 50\%$ cannot exist.

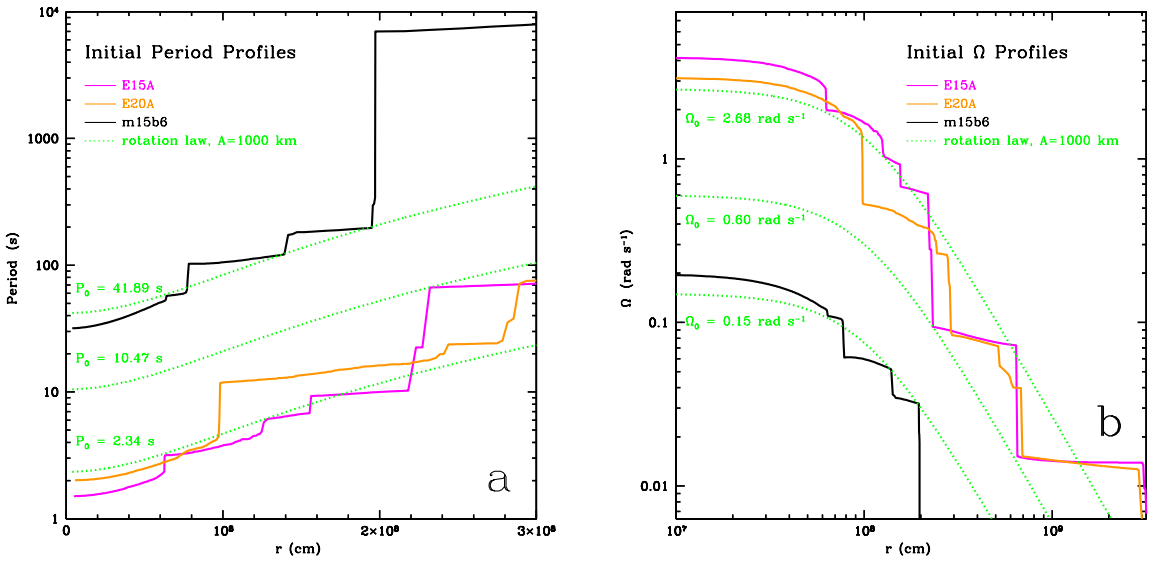

FIG. 1.— Initial rotation period (a) and angular velocity (b) profiles of the rotating progenitor models E15A (magenta), E20A (orange), and m15b6 (black) and of models that are set into rotation according to the rotation law of eq. (1), with A fixed to 1000 km (shown in green for various P_0 or Ω_0). The discontinuities in the E15A, E20A, and m15b6 profiles are connected to compositional interfaces in the rotating progenitors (see Heger et al. 2000).

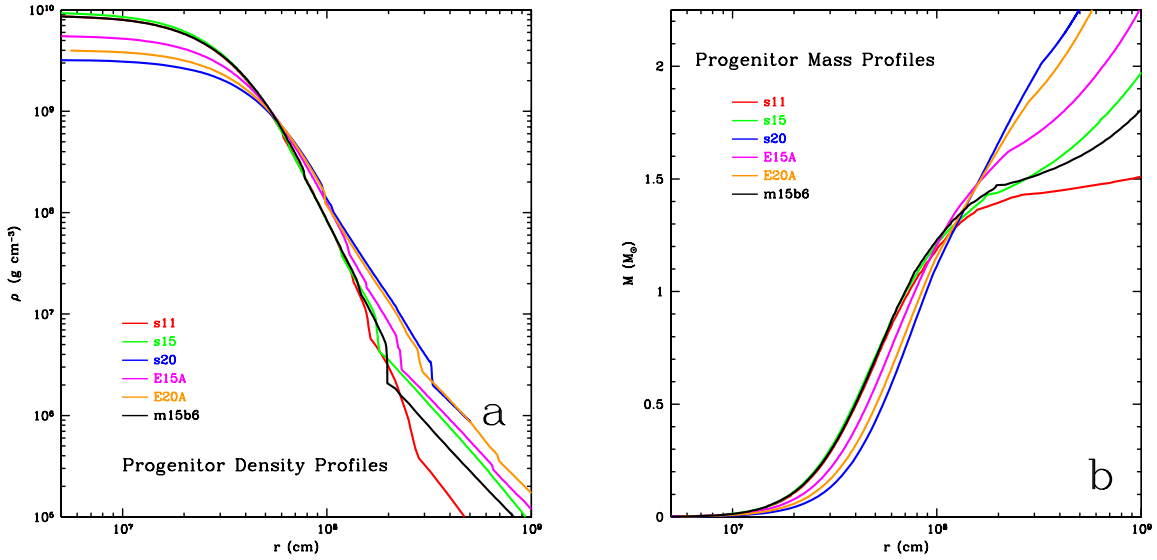

FIG. 2.— Initial mass density profiles (a) and interior mass as a function of radius (b) for all progenitor models used in this study. s11, s15, s20 (11 $M_\odot$, 15 $M_\odot$, and 20 $M_\odot$, respectively) are taken from Woosley & Weaver (1995). Models E15A and E20A (15 $M_\odot$and 20 $M_\odot$) are taken from Heger et al. (2000) and model m15b6 is from Heger et al. (2005). E15A, E20A, and m15b6 were evolved in spherical symmetry with an approximate treatment of centrifugal effects until the end of core carbon burning. Note the great similarity in the density stratifications of models s11, s15, and m15b6, especially interior to ∼2000 km.

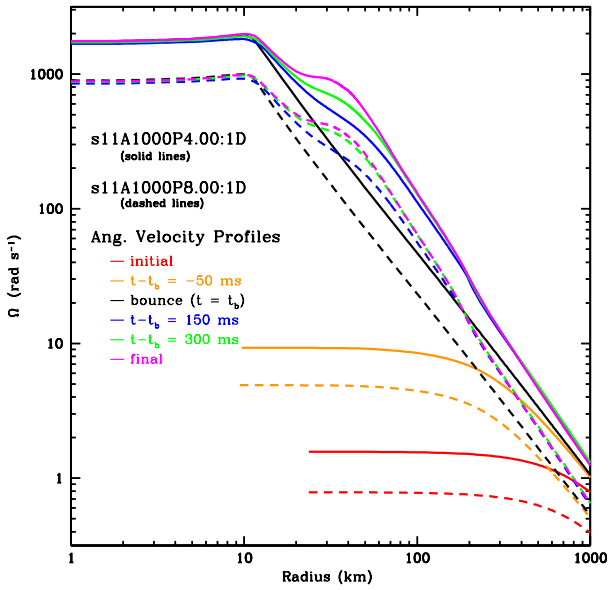

FIG. 3.— Evolution of the angular velocity profile of models s11A1000P4.00:1D (solid lines) and s11A1000P8.00:1D (dashed lines). Both models are initially forced to rotate according to the same rotation law (eq. 1). The initial central period (corresponding to the value of Ω_0; see Table 1) of model s11A1000P8.00:1D is, as indicated by the model name, twice as large as the initial central period of s11A1000P4.00:1D. Note that, due to homologous collapse of the inner core, the solid-body rotation of the central part of the iron core is preserved and the ratio between the central periods remains approximately constant throughout the evolution.

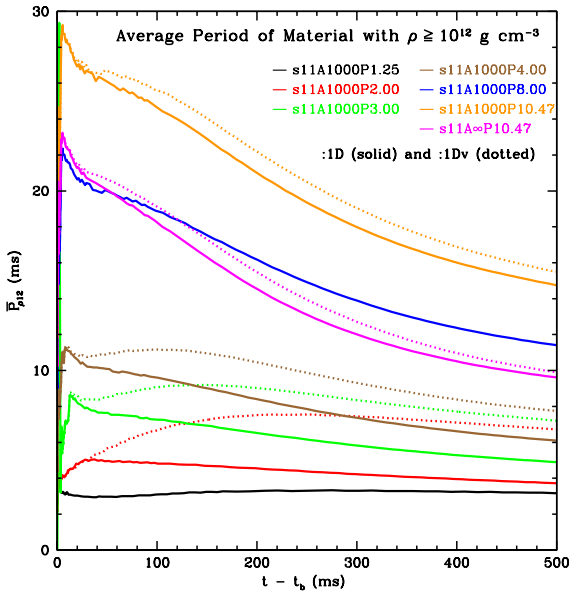

FIG. 4.— Evolution of the moment of inertia-weighted mean period $\bar{P}_{\rho 12}$ for material of density greater than or equal to 10^{12} g cm^{-3} according to eqs. (3) and (2). Shown are selected models of the one-dimensional s11 model series with (dotted lines, :1Dv) and without (solid lines, :1D) viscous dissipation/angular momentum redistribution. For models s11A1000P1.25:1D and s11A1000P8.00:1D, no computation with active viscous dissipation is performed. Viscosity (see §2.1) generically leads to spindown of the protoneutron star. It is most efficient at doing so in fast rotators and in the most extreme case (in model s11A1000P2.00) leads to a final mean period that is twice as large as in the nonviscous case.

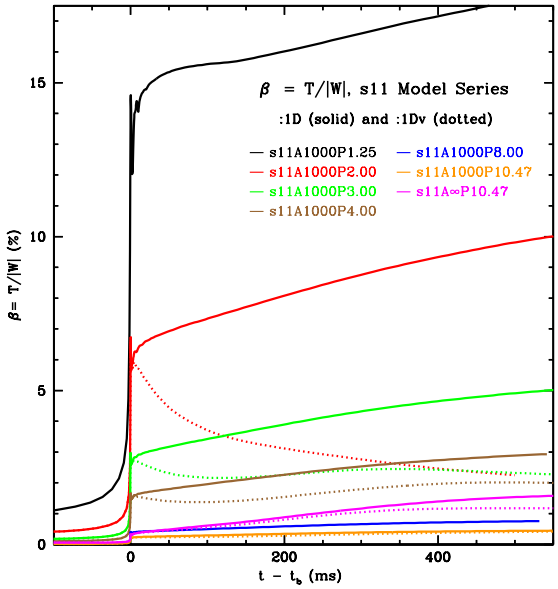

FIG. 5.— Evolution of the rotation parameter $\beta = T/|W|$ for selected models of the s11 model series in 1D. Solid lines: models without viscous dissipation (:1D), dotted lines: models with viscous dissipation (:1Dv). For models s11A1000P1.25:1D and s11A1000P8.00:1D, no computation with active viscous dissipation is performed. Note the strong impact of viscous dissipation acting on the energy stored in differential rotation.

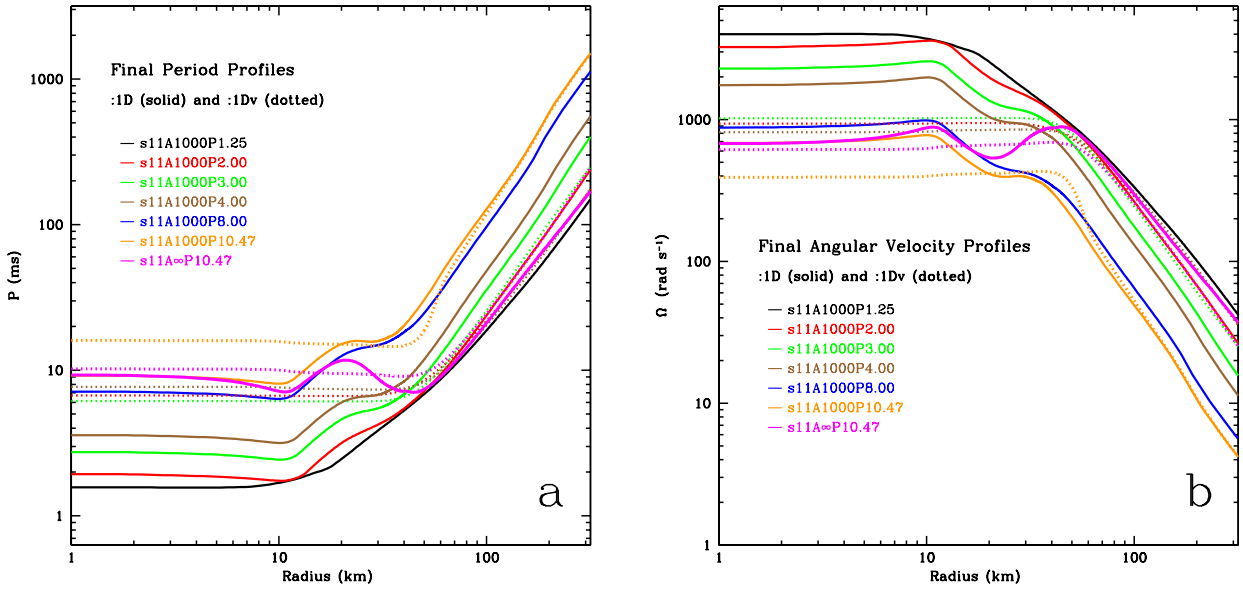

FIG. 6.— Profiles of the period (a) and the angular velocity (b) at the end of each simulation for selected models from the s11 model series, evolved in spherical symmetry with SESAME. The models are initially forced into rotation via the rotation law given in eq. (1) with a choice of $\Omega_0 = 2\pi P_0^{-1}$ and A as specified in the model name. Model graphs plotted in solid lines correspond to spherically symmetric evolution without the inclusion of viscous effects (:1D suffix in Tables 1 and 2). Model graphs plotted in dotted lines correspond to spherically-symmetric evolution with viscous dissipation and angular momentum redistribution (:1Dv suffix in Tables 1 and 2). For models s11A1000P1.25 (black) and s11A1000P8.00 (blue), no :1Dv evolution is carried out. Note the approximate solid-body rotation of all :1D models out to ∼10 km. Also note the factor of 3 to 4 larger region of solid-body rotation realized by viscous dissipation in all :1Dv models.

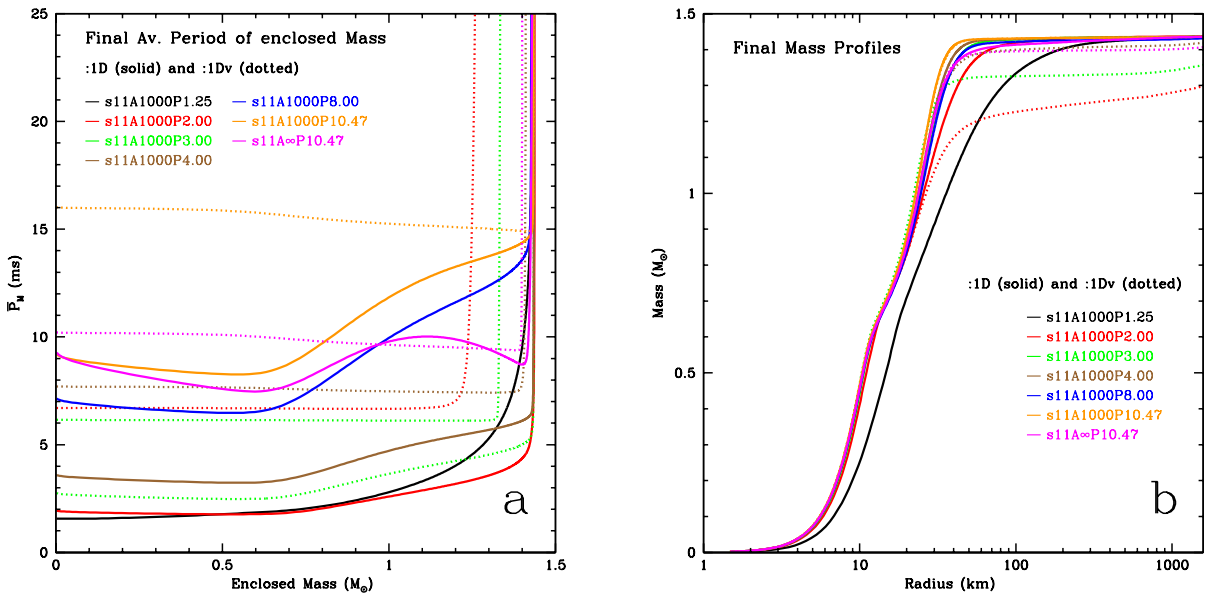

FIG. 7.— (a) Final moment-of-inertia-weighted mean period $\bar{P}_M$ for material interior to a given mass coordinate M and (b) mass M(*R*) contained inside a radius *R*. Both quantities are plotted for a subset of the s11:1D and :1Dv model series at the end of each calculation. The early and strong explosions of models s11A1000P2.00:1Dv and s11A1000P3.00:1Dv lead to significantly smaller PNS masses. This is apparent in plot (b), but also in plot (a), where the lower "mass cut" in $\bar{P}_M$ is obvious. Models s11A1000P1.25:1D and s11A∞P10.47:1D, and their :1Dv variants, also explode, but more weakly and at later times. This is why their profiles do not deviate as much from the models that do not explode. Model s11A1000P1.25:1D is the fastest model that we consider. Due to strong centrifugal forces, s11A1000P1.25:1D's protoneutron star is rather extended (plot b). Also note that the inclusion of dissipative angular momentum redistribution leads to rigid rotation throughout the PNS for all :1Dv models.

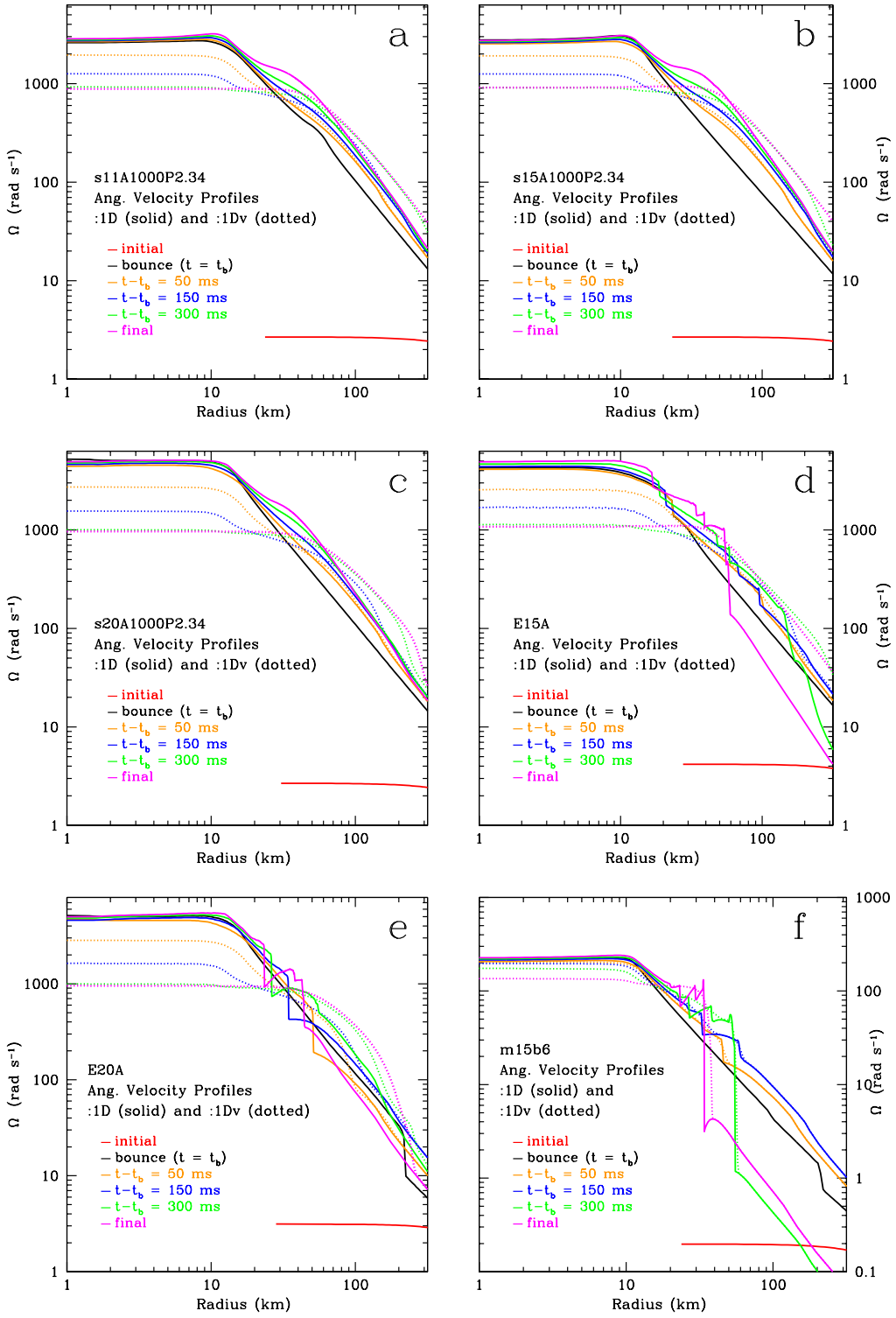

FIG. 8.— Evolution of angular velocity profiles out to ∼300 km. For each model, we plot profiles of the angular velocity at the beginning of the simulation, at bounce, 50 ms, 150 ms, and 300 ms after bounce, as well as the final angular velocity profile at the end of each simulation using SESAME. In each of the panels, we contrast evolution with (dotted lines) and without (solid lines) viscous dissipation and angular momentum redistribution. Note that the dissipative terms are switched on only after bounce. Also, note that, due to the Lagrangean nature of SESAME, initially the innermost mass zone has an inner boundary at ∼25 km. Panel (a) shows the $\Omega(r)$ evolution for models s11A1000P2.34:1D and s11A1000P2.34:1Dv. In panel (b), we display the $\Omega(r)$ evolution of models s11A1000P2.34:1D and s11A1000P2.34:1Dv. Note that the initial progenitor density stratifications of s11 and s15 are very similar (Fig. 2). Hence, using the same values of A and P_0 yields a very similar $\Omega(r)$ evolution. Models s20A1000P2.34:1D and s20A1000P2.34:1Dv (panel c) are set up with the same rotation law as the former models. However, the s20 model is considerably more massive and has a shallower density stratification (see Table 1 and Fig. 2). Panels (d) and (e) show $\Omega(r)$ evolution for models E15A:1D, E15A:1Dv, E20A:1D, and E20A:1Dv. The presupernova models are drawn from the study of Heger et al. (2000) who evolved them with a one-dimensional treatment of rotation. The jumps in the angular velocity profiles are connected with compositional interfaces in the progenitor stars at which the angular velocity jumps. Note how effectively the dissipative mechanism smoothes out these discontinuities in the :1Dv models. Finally, in panel (f), we display the angular velocity profile evolution for the slow, "magnetic" model m15b6 of Heger et al. (2005), which reaches about an order-of-magnitude smaller angular velocities than the other models displayed in this figure.

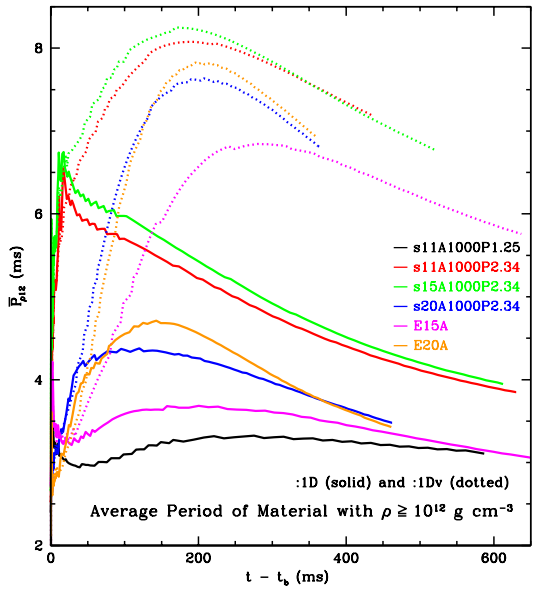

FIG. 9.— Evolution of the moment of inertia-weighted mean period $\bar{P}_{\rho 12}$ for material of density greater than or equal to 10^{12} g cm^{-3} according to eqs. (3) and (2). Shown is a set of models encompassing s11A1000P1.25, s11A1000P2.34, s15A1000P2.34, s20A1000P2.34, E15A, E20A and m15b6 to gauge the influence of progenitor structure on the PNS spin evolution. For each model, with the exception of s11A1000P1.25, we show the :1D (no viscous dissipation and angular momentum transport; solid lines) and :1Dv variants (dotted lines). Note that the range of $\bar{P}_{\rho 12}$ in this figure is different than found in the otherwise similar Fig. 4. The small discontinuities in the graphs are due to individual cells moving above or below the density threshold that is applied for the computation of $\bar{P}_{\rho 12}$.

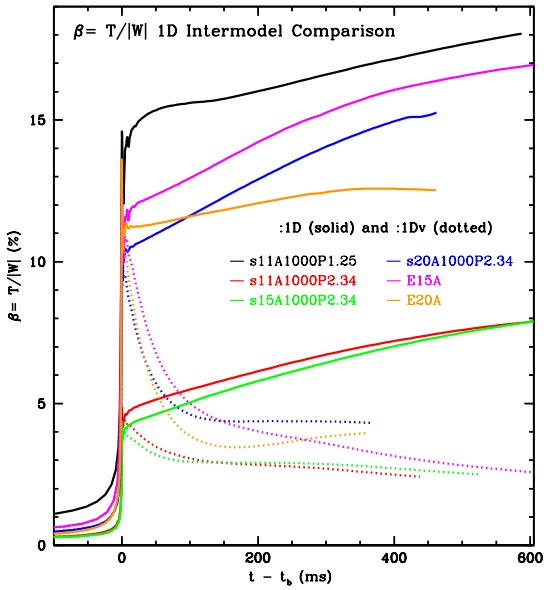

FIG. 10.— Evolution of the rotation parameter $\beta = T/|W|$. We compare models with different progenitor structure. Model variants without viscous dissipation and angular momentum redistribution (:1D) are shown as solid lines. Those with viscous dissipation/angular momentum redistribution (:1Dv) are plotted as dotted lines. For the s11 progenitor, we show s11A1000P1.25:1D (black) and s11A1000P2.34:1D and s11A1000P2.34:1Dv (red). s15A1000P2.34:1D and s15A1000P2.34:1Dv (green) and s20A1000P2.34:1D and s20A1000P2.34:1Dv (blue) use the s15 and s20 progenitors of Woosley & Weaver (1995), respectively. Models E15A:1D and E15A:1Dv and E20A:1D and E20A:1Dv use the presupernova models provided by Heger et al. (2000).

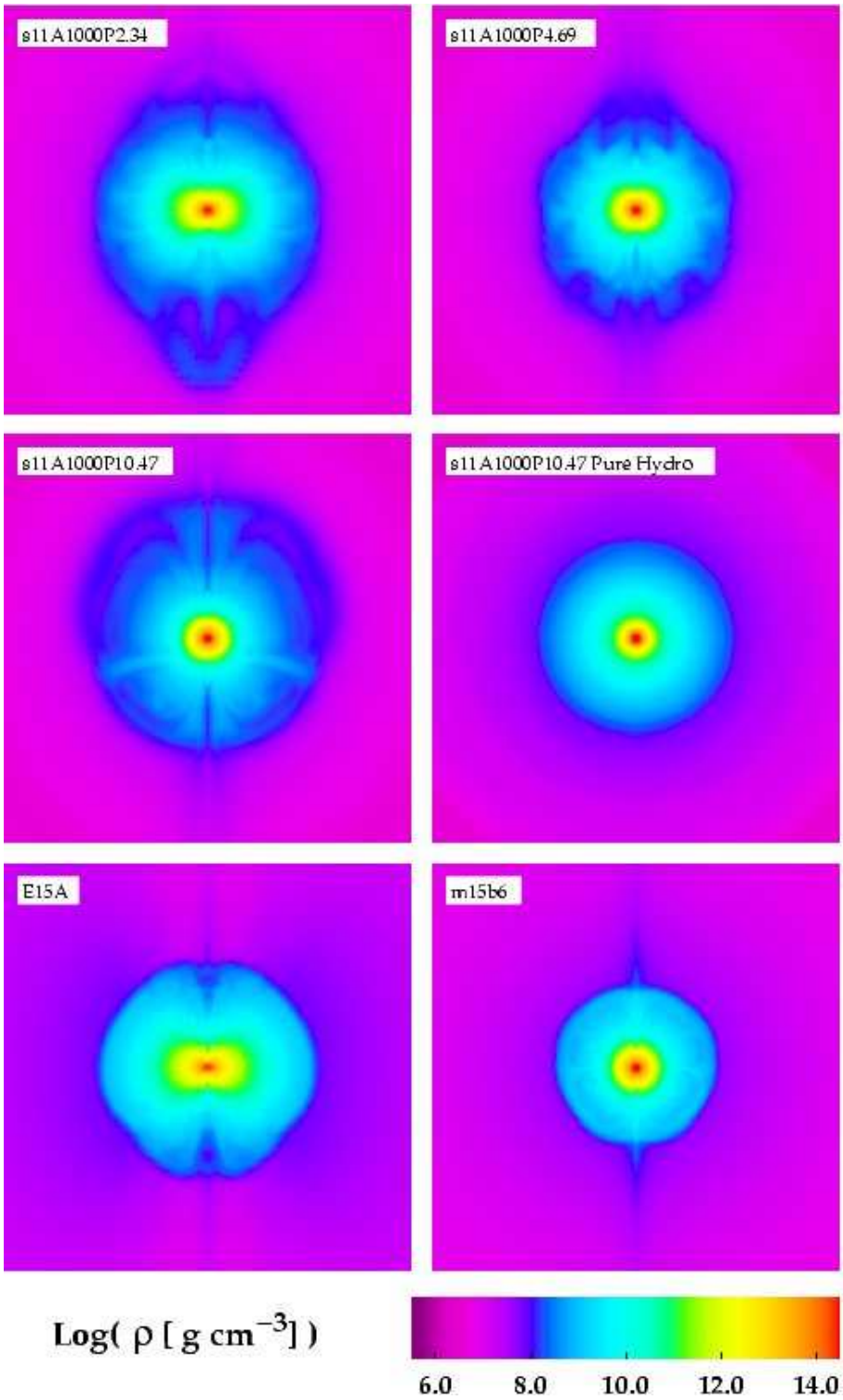

FIG. 11.— Logarithmic color map of the density for a variety of 2D models at 200 ms after core bounce. Shown is the inner 400 km on a side. This figure nicely demonstrates the pronounced rotational flattening of the protoneutron star in fast models (s11A1000P2.34 and E15A). With increasing precollapse iron core period, the PNS becomes less and less rotationally flattened. In models s11A1000P10.47 and m15b6 the flattening has almost disappeared. The lighter cores (s11 models) show considerably stronger convective structure — with the exception of the purely hydrodynamic variant of s11A1000P10.47 — than the more massive cores (E15, m15b6) at 200 ms after bounce. The slight "dents" and "spikes" along the rotation axis are artefacts of the imperfect symmetry axis treatment. Note that the pure hydro variant of s11A1000P10.47 was evolved with an updated version of the VULCAN/2D with improved axis treatment.

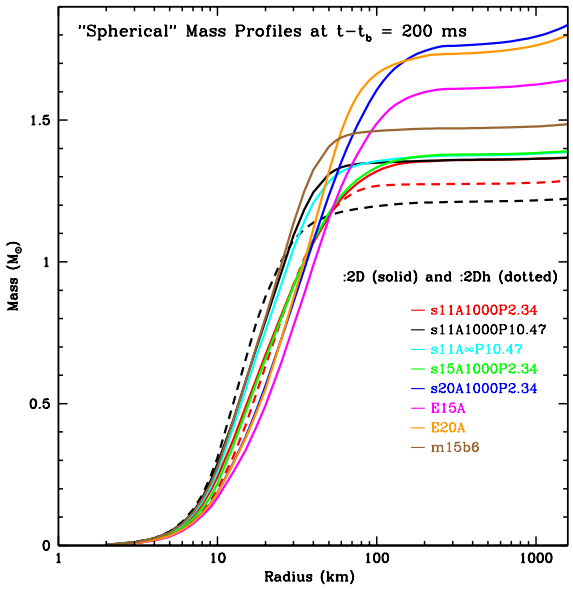

FIG. 12.— Mass contained inside a sphere of radius R for selected two-dimensional models ∼200 ms after core bounce. The "s" models (Woosley & Weaver 1995) with P_0 = 2.34 s and the fast E15A and E20A models (see model parameter details in Table 1) deviate significantly from spherical symmetry. Their spherical mass profiles should, hence, be taken with caution. Solid lines represent mass profiles of MGFLD models. Dashed lines correspond to models which are evolved purely hydrodynamically and experience prompt explosions that blast away the outer core.

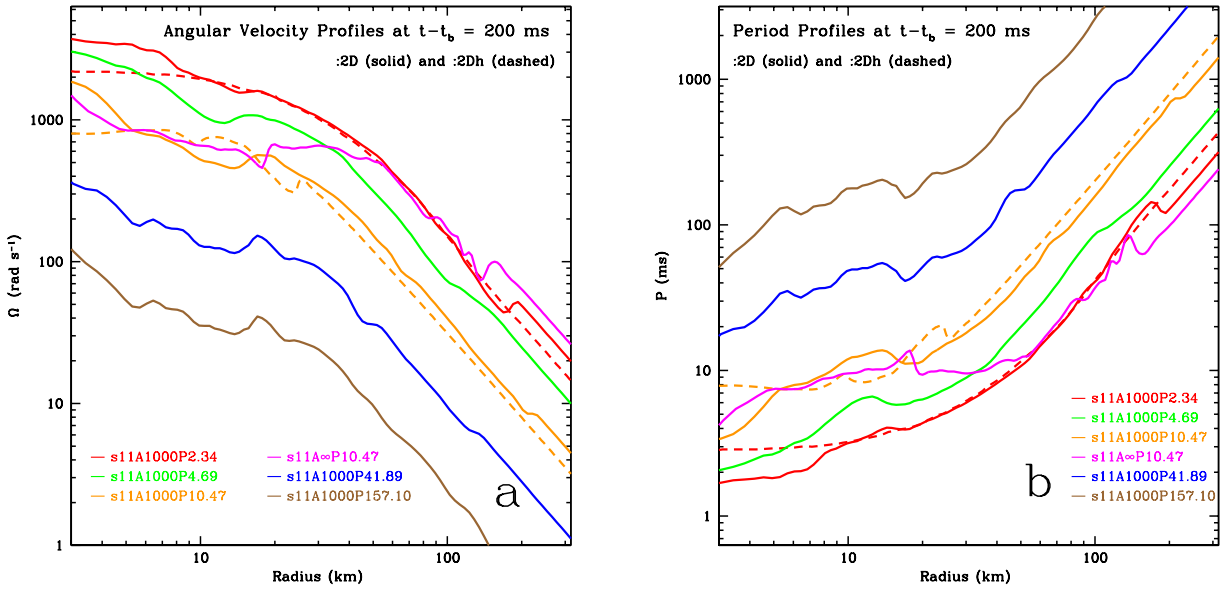

FIG. 13.— Equatorial profiles of the angular velocity (a) and the period (b) at 200 ms after bounce for each model of our s11:2D model series. The two-dimensional PNSs exhibit a low degree of differential rotation inside ∼20 km and then become strongly differentially rotating further out. All s11A1000:2D models exhibit the same qualitative features. Model s11∞P10.47 (initial solid-body rotation), however, differs from its A = 1000 km counterpart. Its PNS is appreciably less compact and the region of quasi-solid-body rotation is more extended. The dashed lines correspond to models that are evolved adiabatically. These models promptly explode and do not undergo a phase of strong convection. Hence, their equatorial profiles show less structure. The profiles are plotted from 3 km on outwards. Due to the imperfect axis treatment in the version of VULCAN/2D that is used for these calculations, we do not highlight the angular velocity and period data inside ∼3 km.

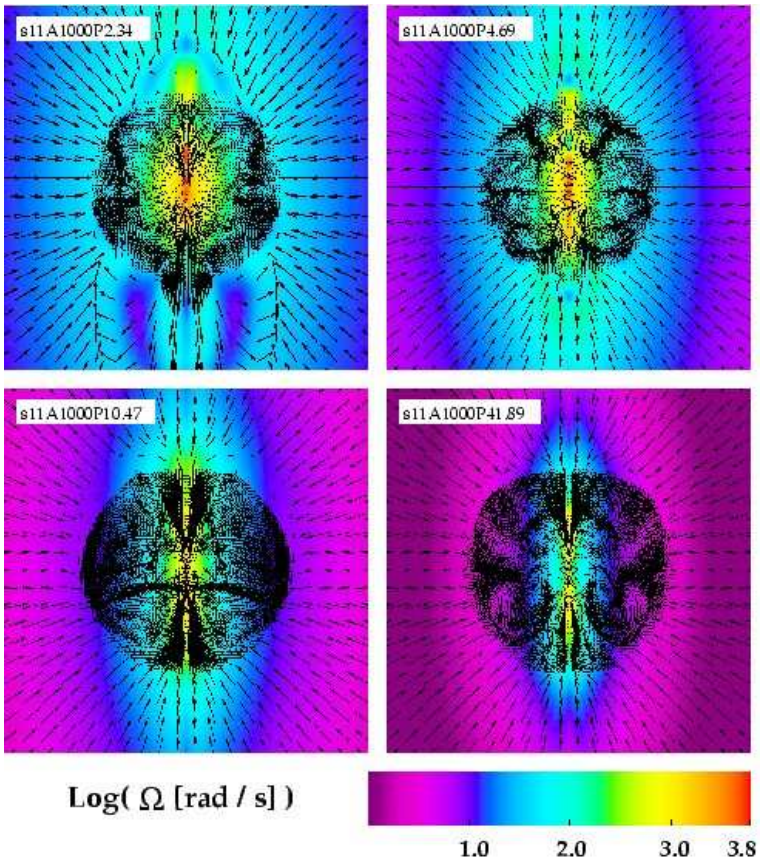

FIG. 14.— Logarithmic color map of the angular velocity Ω for models of our s11A1000:2D model series evolved in axisymmetry using VULCAN/2D with P_0 = 2.34 s, 4.69 s, 10.47 s, and 41.69 s, corresponding to Ω_0 = 2.68 rad s^{-1}, 1.34 rad s^{-1}, 0.60 rad s^{-1}, 0.15 rad s^{-1}. Shown are the inner 400 km on a side. Fluid velocity vectors are superposed. The vector data are downsampled at radii larger than $\sim$200 km. The panels show the angular velocity distribution at about 200 ms after bounce in each model. The fastest model, s11A1000P2.34:2D, has a large centrifugally supported region of high angular-velocity material. This region grows increasingly smaller with increasing initial iron core period. The color map has been artificially limited to a maximum of $10^{3.8}$ rad s^{-1} to cut out unphysically large angular velocities in the zones very close to the rotation axis.

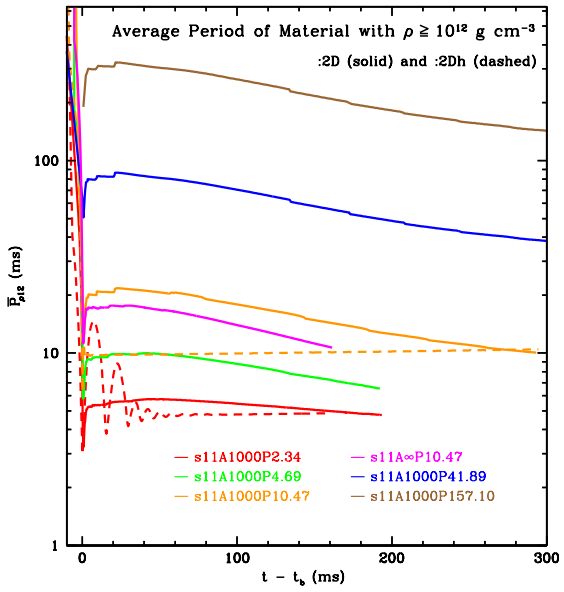

FIG. 15.— Postbounce evolution of the moment of inertia-weighted mean period $\bar{P}_{\rho 12}$. Solid-line graphs depict standard models of the s11A1000:2D model series. Plotted with the dashed lines are the $\bar{P}_{\rho 12}$ of models that were evolved purely hydrodynamically. As expected, all $\bar{P}_{\rho 12}$ exhibit a local minimum at bounce when the inner core is most compact. $\bar{P}_{\rho 12}$ increases slightly after bounce, but ultimately decreases as more material settles onto the contracting PNS. With increasing initial iron core spin period, $\bar{P}_{\rho 12}$ increases systematically. The purely hydrodynamic models' PNSs cannot contract. Hence, their $\bar{P}_{\rho 12}$ s stay constant or increase slightly as lower angular momentum material settles above the density threshold. The fast pure hydro model (P_0 = 2.34 s) exhibits strong postbounce oscillations like those described in the study of Ott et al. (2004). Such oscillations are critically damped in simulations including adequate neutrino treatment.

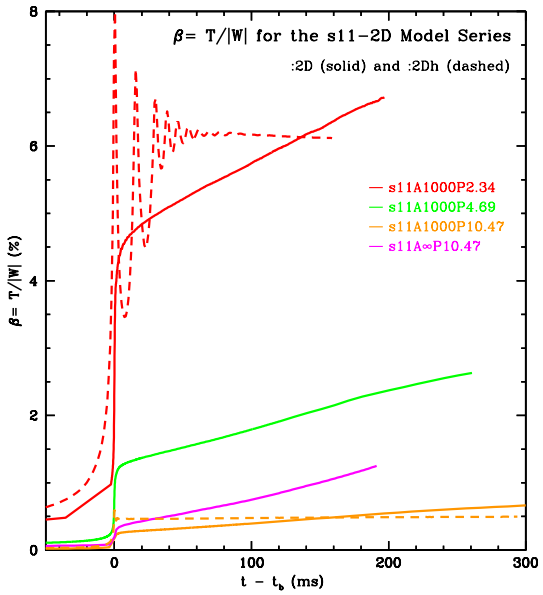

FIG. 16.— Evolution of the rotation parameter β = T/|W| at postbounce times for a subset of the s11A1000:2D model series. β increases dramatically at bounce and increases monotonically, but linearly after bounce in all MGFLD models, because of angular momentum conservation (and hence spin-up) of material that settles down onto the PNS. The slope of β increases with decreasing precollapse spin period. Despite having the same initial spin (P_0 = 10.47 s), model s11A∞P10.47:2D, which is initially in solid-body rotation, reaches higher postbounce βs than model s11A1000P10.47:2D. This is clearly related to the greater total angular momentum in the former. Model s11A1000P2.34-2Dh's β evolution reflects this model's large-scale coherent postbounce oscillations. Both :2Dh models evolve to constant β, both because they explode and because their PNSs cannot contract and spin up.

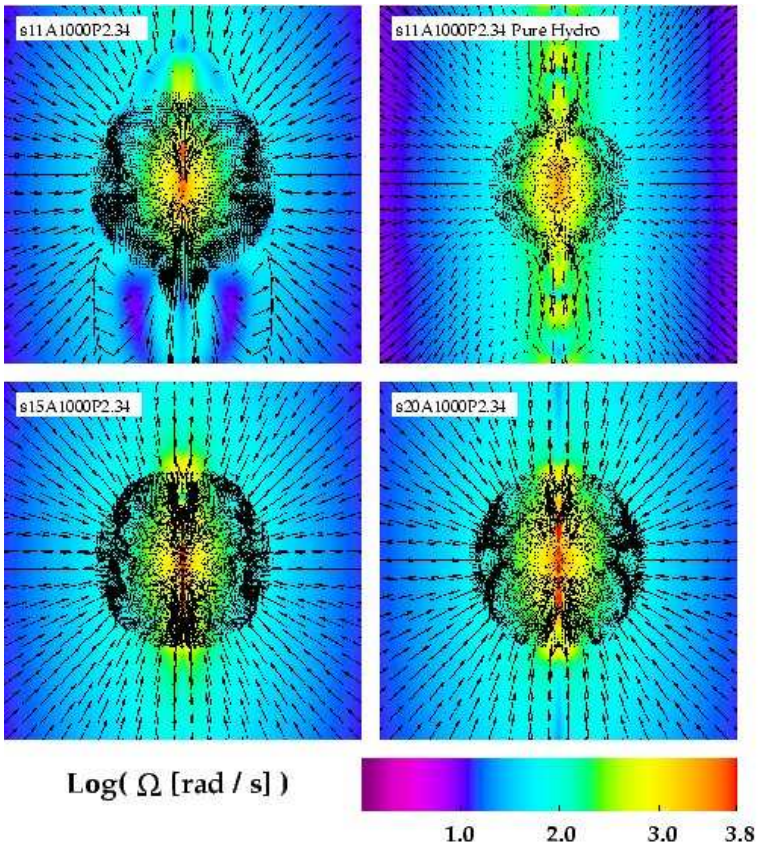

FIG. 17.— Logarithmic color map of the angular velocity distribution in models s11A1000P2.34:2D, s11A1000P2.34:2Dh, s15A1000P2.34:2D, and s20A1000P2.34:2D. Shown are the inner 400 km on a side at 200 ms after bounce (150 ms for s11A1000P2.34:2Dh). Velocity vectors are superposed in the same way as in Fig. 14. Model s11A1000P2.34:2Dh is evolved purely hydrodynamically. It explodes and leaves behind a less compact configuration with smaller central Ω than the corresponding model with MGFLD. With increasing progenitor iron core mass (Table 1), the magnitude of the final angular velocity increases and its distribution becomes broader.

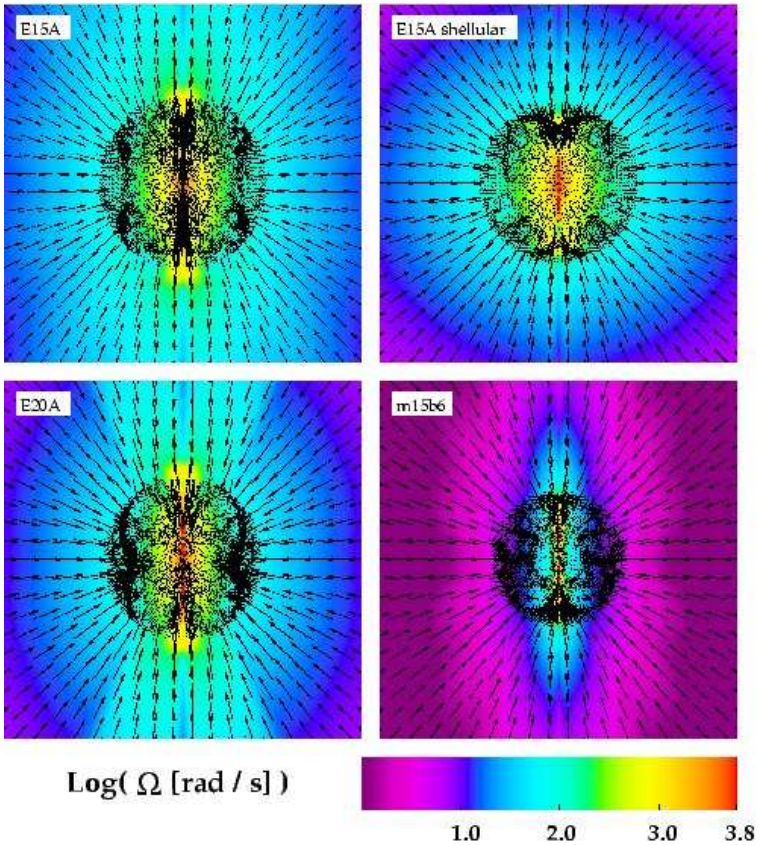

FIG. 18.— Logarithmic color map of the angular velocity of models E15A:2D, E15A:2Ds ("shellular rotation"), E20A:2D and m15b6:2D which use the rotating progenitors of Heger et al. (2000) and Heger et al. (2005). Shown are the inner 400 km on a side at 200 ms after core bounce. Velocity vectors are superposed and downsampled at radii greater than about 200 km. The :2Ds variant of E15A is initially set up to rotate with constant Ω on spherical shells. Its region of high angular velocity is more compact than in its :2D counterpart, which is initially set up to rotate with constant angular velocity on cylindrical shells. Interestingly, the innermost regions of E15A:2D and E15A:2Ds are quite similar. Model E20A:2D has a more massive core than model E15A:2D, but slower initial rotation. Its central angular momentum distribution is very similar to the one seen in E15A:2D. Model m15b6:2D has a high initial period of $\sim$32 s.

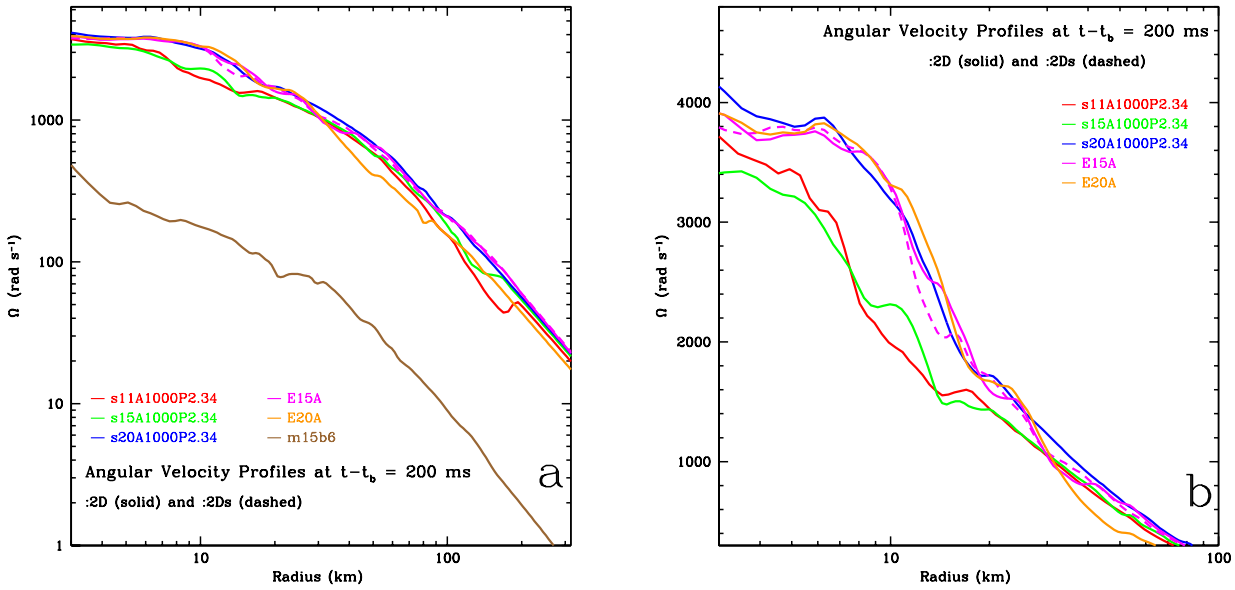

FIG. 19.— Equatorial profiles of the angular velocity at 200 ms after bounce for a set of models with similar initial iron core periods (P_0) and different progenitor mass. The slow "magnetic" model m15b6 (Heger et al. 2005) stands out and has been included in (a) for comparison. (a) shows Ω on a logarithmic scale vs. radius and (b) displays Ω on a linear scale for the innermost 100 km of each model. On a logarithmic scale it is hardly possible to distinguish between individual fast models. With the exception of s11 and s15 that have very similar progenitor structure, more massive progenitors lead to slightly higher PNS central Ω. The model E15A:2Ds (dashed-magenta graph) is setup in "shellular" rotation. This, however, does not lead to a considerably different equatorial Ω profile at postbounce times than that of model E15A:2D. Differences in off-equatorial regions are, however, present (see Fig. 18).

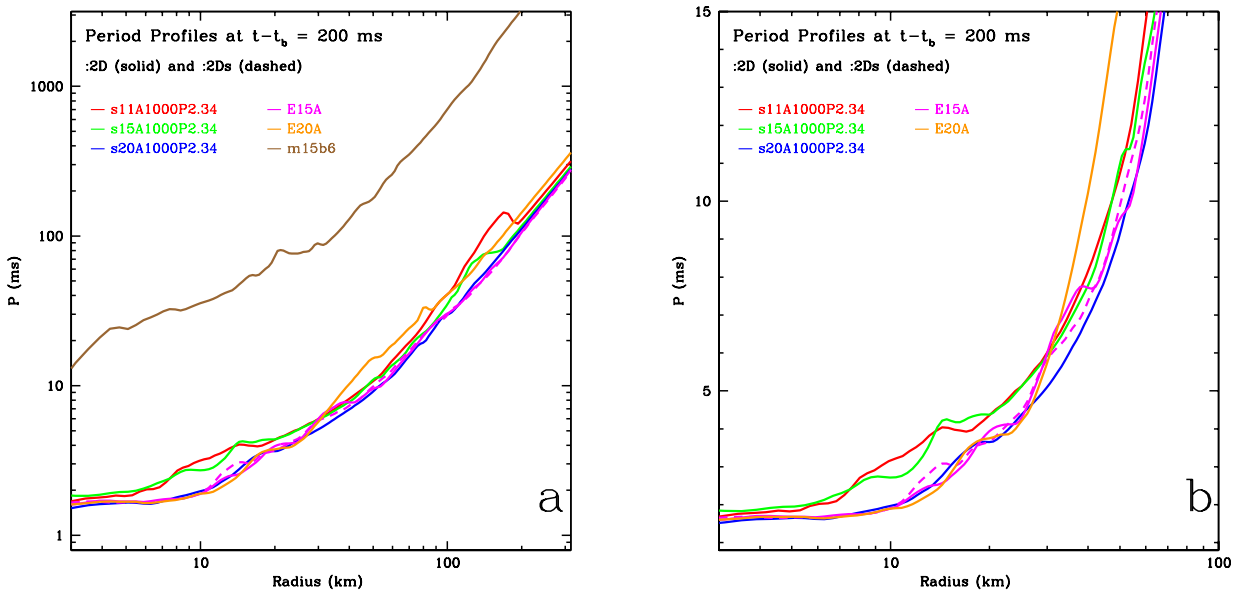

FIG. 20.— Equatorial profiles of the rotation period at 200 ms after bounce for the same set of models displayed in Fig. 19. (a) and (b) display P on logarithmic and linear scales, respectively. Note the very similar central periods of all "fast" models.

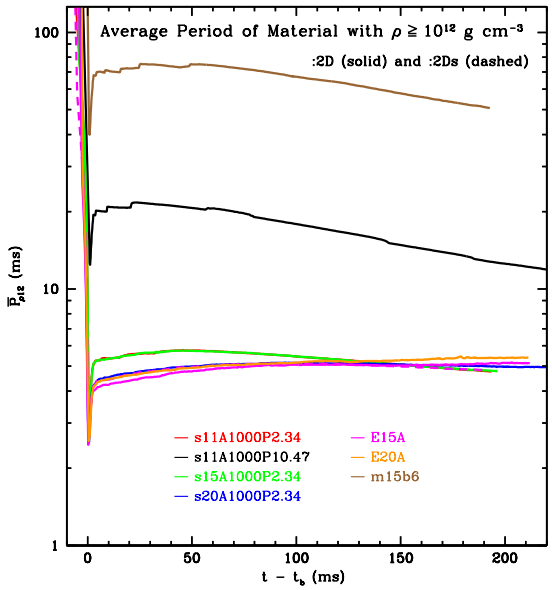

FIG. 21.— Postbounce evolution of the moment of inertia-weighted mean period $\bar{P}_{\rho 12}$ for models with differing initial iron core spin and progenitor mass. $\bar{P}_{\rho 12}$ strongly depends on the initial iron core spin and weakly on progenitor mass and structure. Interestingly, the choice of rotation law ("cylindrical" vs. "shellular" — see dashed plot for E15A:2Ds) has little effect on the mean period. The small discontinuities in some of the graphs at early postbounce times are due to the finite resolution of our numerical grid and occur when an entire mass shell first exceeds the density threshold ($\rho \geq 10^{12}$ g cm^{-3}).

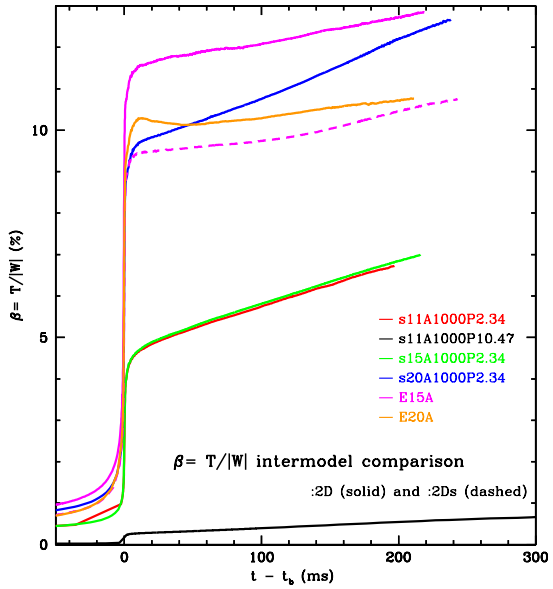

FIG. 22.— Evolution of the rotation parameter β = T/|W|. Here, we compare a representative set of models from our two-dimensional model series. Due to the similarity of their progenitor structures, s11A1000:2D and s15A1000:2D have almost identical β evolutions for the same initial iron core spin period (red and green graphs). β increases linearly after bounce in all Woosley & Weaver (1995) models. Models E15A:2D, E15A:2Ds, and E20A:2D have considerably more complicated rotational structures (Fig. 1). Hence, an appreciably different β evolution can be expected ($T \propto \Omega^2$). Model s20A1000P2.34 shows the steepest β slope and is likely to reach the classical limit for secular rotational instability ($\beta \geq 14$ %). However, a low-T/|W| instability might set in at much lower β (Ott et al. 2005).

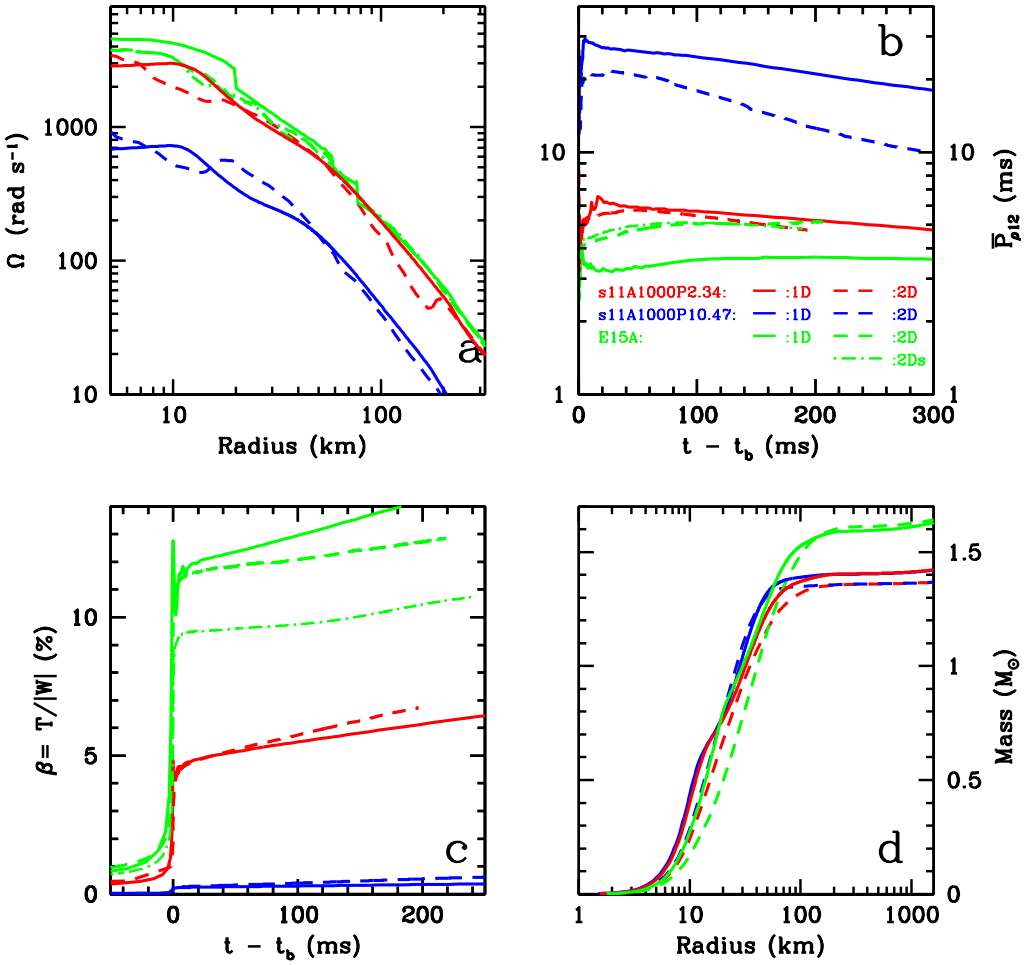

FIG. 23.— Contrasting one-dimensional to two-dimensional results: In panel (a), the equatorial angular velocity profiles at 200 ms after bounce of three models, namely s11A1000P2.34 (red), s11A1000P10.47 (blue), and E15A (green), each in spherical symmetry (solid lines) and axisymmetry (dashed lines), are compared. The profiles are plotted from 5 km on outwards to excise axis artefacts. For E15A:2D, we also plot the "shellular" variant. Panel (b) shows the evolution of the moment-of-inertia weighted mean period $\bar{P}_{\rho 12}$ for the selected set of models. In Panel (c), we display the evolution of the rotation parameter β and panel (d) depicts the mass-(spherical)radius relationship at 200 ms after bounce.

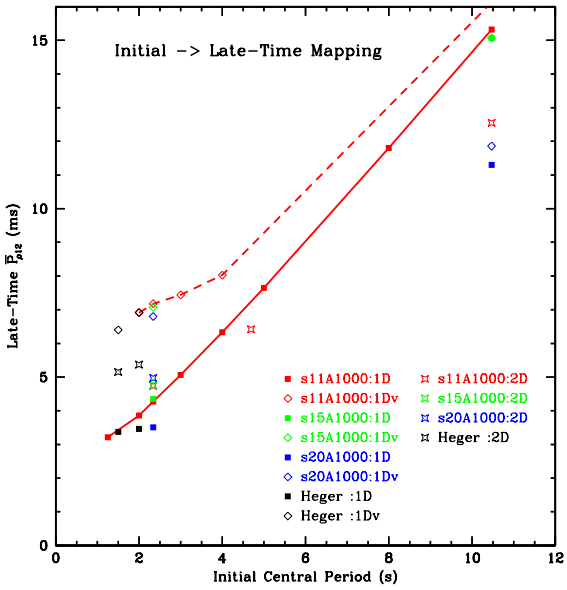

FIG. 24.— Mapping from the initial central iron core spin period to the mean PNS period at ∼450 ms after bounce for the one-dimensional and ∼200 ms after bounce for the two-dimensional models. We choose these times for consistency among models from each model set. Most two-dimensional models are evolved beyond ∼200 ms after bounce while most one-dimensional models are evolved beyond ∼450 ms after bounce (see Tables 2 and 3). On the abscissa, we plot the initial central period in seconds and on the ordinate we plot the moment-of-inertia-weighted mean period of the PNS. Models evolved with radiation-hydrodynamics in spherical symmetry are marked by solid boxes. Spherically-symmetric models that include viscosity are marked by open rhombi. Open stars symbolize axisymmetric models. In addition, the model icons are color-coded according to their progenitor type. s11 models are represented by red, s15 by green, and s20 by blue. Models from the recent studies of Heger et al. (2000) and Heger et al. (2005) are marked black. For the models considered in this study, rotational effects are not dominant and the mapping between initial and final rotation period is approximately linear.

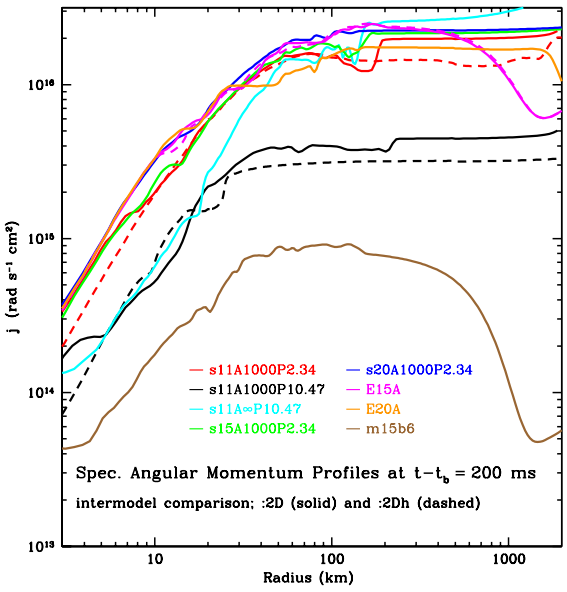

FIG. 25.— Equatorial specific angular momentum (j) profiles at 200 ms after core bounce plotted for a representative set of models evolved in axisymmetry with VULCAN/2D. Drawn in solid lines are graphs of models evolved with MGFLD and dashed lines represent models that are evolved purely hydrodynamically and undergo prompt explosions. At 200 ms after bounce, the PNS is already relatively compact and most of the mass on the grid is located interior to ∼50 km (Fig. 12). Models that make use of the E15A, E20A (Heger et al. 2000), and m15b6 (Heger et al. 2005) presupernova models show drops in their j profiles at large radii which correspond to the discontinuities in their precollapse rotational profiles (Fig. 1).